Astronomy & Astrophysics

BUFFALO/Flashlights: Constraints on the abundance of lensed supergiant stars in the Spock galaxy at redshift 1

Jose M. Diego[1], Sung Kei Li[2], Ashish K. Meena[3], Anna Niemiec[4], Ana Acebron[5,6], Mathilde Jauzac[7,8,9,10], Mitchell F. Struble[11], Alfred Amruth[2], Tom J. Broadhurst[13,14,15], Catherine Cerny[7,8], Harald Ebeling[16], Alexei V. Filippenko[17], Eric Jullo[18], Patrick Kelly[19], Anton M. Koekemoer[20], David Lagattuta[7,8], Jeremy Lim[2], Marceau Limousin[18], Guillaume Mahler[7,8], Nency Patel[8], Juan Remolina[21], Johan Richard[22], Keren Sharon[21], Charles Steinhardt[23], Keiichi Umetsu[24], Liliya Williams[25], Adi Zitrin[3], Jose María Palencia[1], Liang Dai[26], Lingyuan Ji[26], and Massimo Pascale[17,12]

[1] Instituto de Física de Cantabria (CSIC-UC), Avda. Los Castros s/n, 39005 Santander, Spain
e-mail: jdiego@ifca.unican.es
[2] Department of Physics, The University of Hong Kong, Pokfulam Road, Hong Kong
[3] Physics Department, Ben-Gurion University of the Negev, PO Box 653, Be'er-Sheva 84105, Israel
[4] LPNHE, CNRS/IN2P3, Sorbonne Université, Université Paris-Cité, Laboratoire de Physique Nucléaire et de Hautes Énergies, 75005 Paris, France
[5] Department of Physics of the University of Milano, via Celoria 16, 20133 Milano, Italy
[6] INAF – IASF Milano, via A. Corti 12, 20133 Milano, Italy
[7] Center for Extragalactic Astronomy, Durham University, South Rd, Durham DH1 3LE, UK
[8] Institute for Computational Cosmology, Durham University, South Road, Durham DH1 3LE, UK
[9] Astrophysics Research Center, University of KwaZulu-Natal, Westville Campus, Durban 4041, South Africa
[10] School of Mathematics, Statistics & Computer Science, University of KwaZulu-Natal, Westville Campus, Durban 4041, South Africa
[11] Department of Physics and Astronomy, University of Pennsylvania, 209 South 33rd Street, Philadelphia, PA 19104, USA
[12] Department of Physics, University of Hong Kong, Hong Kong, Hong Kong SAR
[13] Department of Physics, University of the Basque Country UPV/EHU, 48080 Bilbao, Spain
[14] DIPC, Basque Country UPV/EHU, 48080 San Sebastian, Spain
[15] Ikerbasque, Basque Foundation for Science, 48011 Bilbao, Spain
[16] Institute for Astronomy, University of Hawaii, 640 N Aohoku Pl, Hilo, HI 96720, USA
[17] Department of Astronomy, University of California, Berkeley, CA 94720-3411, USA
[18] Aix-Marseille Univ., CNRS, CNES, LAM, 13388 Marseille, France
[19] Minnesota Institute for Astrophysics, University of Minnesota, 116 Church Street SE, Minneapolis, MN 55455, USA
[20] Space Telescope Science Institute, 3700 San Martin Dr., Baltimore, MD 21218, USA
[21] Department of Astronomy, University of Michigan, 1085 S. University Ave, Ann Arbor, MI 48109, USA
[22] Univ. Lyon, ENS de Lyon, CNRS, Centre de Recherche Astrophysique de Lyon UMR5574, 69230 Saint-Genis-Laval, France
[23] Niels Bohr Institute, University of Copenhagen, Lyngbyvej 2, København Ø 2100, Denmark
[24] Institute of Astronomy and Astrophysics, Academia Sinica (ASIAA), AS/NTU Astronomy-Mathematics Building, No. 1, Sec. 4, Roosevelt Rd., Taipei 10617, Taiwan
[25] School of Physics and Astronomy, University of Minnesota, 116 Church Street, Minneapolis, MN 55455, USA
[26] Department of Physics, University of California, 366 Physics North MC 7300, Berkeley, CA 94720, USA

ABSTRACT

In this work, we present a constraint on the abundance of supergiant (SG) stars at redshift $z \approx 1$, based on recent observations of a strongly lensed arc at this redshift. First we derived a free-form model of MACS J0416.1-2403 using data from the Beyond Ultra-deep Frontier Fields and Legacy Observations (BUFFALO) program. The new lens model is based on 72 multiply lensed galaxies that produce 214 multiple images, making it the largest sample of spectroscopically confirmed lensed galaxies on this cluster. The larger coverage in BUFFALO allowed us to measure the shear up to the outskirts of the cluster, and extend the range of lensing constraints up to ~1 Mpc from the central region, providing a mass estimate up to this radius. As an application, we make predictions for the number of high-redshift multiply lensed galaxies detected in future observations with the *James Webb* Space Telescope (JWST). Then we focus on a previously known lensed galaxy at $z = 1.0054$, nicknamed Spock, which contains four previously reported transients. We interpret these transients as microcaustic crossings of SG stars and explain how we computed the probability of such events. Based on simplifications regarding the stellar evolution, we find that microlensing (by stars in the intracluster medium) of SG stars at $z = 1.0054$ can fully explain these events. The inferred abundance of SG stars is consistent with either (1) a number density of stars with bolometric luminosities beyond the Humphreys-Davidson (HD) limit ($L_{max} \approx 6 \times 10^5 \, L_\odot$ for red stars), which is below ~400 stars kpc^{-2}, or (2) the absence of stars beyond the HD limit but with a SG number density of ~9000 kpc^{-2} for stars with luminosities between $10^5 \, L_\odot$ and $6 \times 10^5 \, L_\odot$. This is equivalent to one SG star per 10×10 pc^2. Finally, we make predictions for future observations with JWST's NIRcam. We find that in observations made with the $F200W$ filter that reach 29 mag AB, if cool red SG stars exist at $z \approx 1$ beyond the HD limit, they should be easily detected in this arc.

Key words. gravitation – gravitational lensing: strong – supergiants

1. Introduction

The galaxy cluster MACS J0416.1-2403 (MACS0416 hereinafter; Mann & Ebeling 2012) at redshift $z = 0.396$ is one of the six clusters studied with exquisite detail by the *Hubble* Space Telescope (HST) as part of the *Hubble* Frontier Field (HFF) program. It was selected based on its prominent lensing signature (Zitrin et al. 2013). During this program, HST observed $\sim 10\,\mathrm{arcmin}^2$ around the central portion of the cluster in wavelengths ranging from $0.45\,\mu m$ to $1.6\,\mu m$ and to a depth of ~ 28.5 mag in the optical and infrared (IR) bands. The HFF data from MACS01416 have been extensively used by lens modelers (Jauzac et al. 2014, 2015; Johnson et al. 2014; Diego et al. 2015; Kawamata et al. 2016; Hoag et al. 2016; Caminha et al. 2017; Richard et al. 2021; Bergamini et al. 2023) in the search for high-redshift galaxies (McLeod et al. 2015; Oesch et al. 2015; Kawamata et al. 2016; Ishigaki et al. 2018), and for the discovery of some of the first lensed stars beyond $z = 0.9$ (Rodney et al. 2018; Chen et al. 2019; Kaurov et al. 2019).

One of the goals of the HFF program was to find the most distant galaxies, taking advantage of the magnifying boost given by the gravitational lensing effect. The frequency coverage of HST allows one to potentially detect galaxies up to $z \approx 12$ thanks to the dropout technique (Steidel et al. 1999). The census of these high-redshift galaxies has provided useful information about the evolution of the ultraviolet (UV) luminosity function with redshift. However, the number of galaxies at the highest redshifts remains low, resulting in large uncertainties in the luminosity function. In order to increase the statistics, the Beyond Ultra-deep Frontier Fields and Legacy Observations (BUFFALO) program doubles the area around these clusters that is being covered by the IR detectors. In addition, the extended area around the central region of the clusters allows us to complement the strong-lensing constraints with weak-lensing measurements. The addition of weak lensing in the external parts of the cluster is important because it helps to reduce the uncertainty in the magnification, which is vital to properly derive the luminosity functions of distant lensed galaxies observed around this cluster.

MACS0416 is so far the most remarkable cluster in terms of the number of transient events, allegedly due to microlensing. This is mostly owed to the existence of two galaxies at $z \approx 1$ that are crossing the cluster caustic. Earlier HST observations have revealed at least six transient events in these two galaxies (Rodney et al. 2018; Chen et al. 2019; Kaurov et al. 2019; Kelly et al. 2022), with all of them consistent with being microlensing events[1]. The low redshift of these two caustic-crossing galaxies is one of the reasons behind the wealth of microlensing events of distant stars detected in this cluster. More abundant but fainter stars can be promoted by lensing beyond the detection limit with typical microlensing magnification factors of several thousand. To detect similar stars in more distant galaxies at $z \approx 2$ or beyond would require more extreme (and less likely) magnification factors in order to compensate for the increase in luminosity distance. Because of this, MACS0416 can be referred to as the "Christmas tree galaxy cluster" owing to the large number of flickering microlensing events detected behind this cluster. The main focus of this paper is to study these microlensing events in one of the two galaxies, the Spock galaxy at $z = 1.0054$ (Rodney et al. 2018; Kelly et al. 2022) which shows four microlensing events in HST data.

Given the interconnection between the microlensing events and the macromodel magnification, we divide this paper into several parts. First we discuss a new lens macromodel derived using the latest HST data from the BUFFALO program, and then we study the population of luminous stars in the Spock galaxy in more detail. Finally, we explore how microlenses in the cluster help the transients observed in this arc to be interpreted as microlensing events of the most luminous stars in the Spock galaxy.

Two of the transient events were found as part of the FrontierSN program (HST-PID 13386; PI S. Rodney), and the other two as part of the Flashlights program (Kelly et al. 2022). The FrontierSN program (Rodney 2014) is designed to produce light curves of supernovae (SNe), so it has a natural good cadence of ~ 1 observation per day during a period of ~ 1 month. The Flashlights program (Kelly et al. 2019) is designed to find flux variations of unresolved objects, and to accomplish this, it makes two deep observations with HST with the same position angle (so subtracted images minimize instrumental effects) using very wide filters (to reach fainter objects). The Flashlights program has proven to be the most successful at finding lensed star candidates with HST, with over two dozen candidates found in the HFF clusters (see Kelly et al. 2022, for a detailed description of the program and main results). The transients in the Spock arc have been interpreted as possible microlensing events of distant stars in the galaxy at $z = 1.0054$, which are temporarily being magnified by stars in the cluster (at $z = 0.396$). Other possible interpretations for the transients are considered by Rodney et al. (2018) – for instance, luminous blue variable (LBV) stars or recurrent novae –, but in this work we adopt the hypothesis that the transient nature of these events is due to changes in the magnification produced by microlensing. This choice is motivated by the fact that we do not know if these stars are intrinsically variable (LBV or nova), although many luminous stars are. However, we do know that microlenses in the lens plane are relatively numerous in this portion of the lens (from the observed intracluster light), so microlensing events are expected (Diego et al. 2018).

As shown in Fig. 1, the observed photometry during the maximum observed luminosity is also consistent with the hypothesis that the two events of Rodney et al. (2018) are very luminous stars undergoing microlensing episodes near the critical curve of the cluster. In particular, we find that one of the events is well described by a red supergiant (SG) star, while the other one is better described by a hotter SG star. Data points shown in this figure correspond to the measured photometry around the position of maximum luminosity. The photometry in the $F606W$ filter (0.6 micron) has been corrected to account for the fact that this data point corresponds to 1 day (a half day in the rest frame) before maximum luminosity. The two events from the Flashlights program were obtained with a wide filter, so we do not have color information that can be used to test the star hypothesis by comparing the photometry with stellar models.

Under the microlensing hypothesis, the stars that one expects to detect are very luminous ($L > 10^4\,L_\odot$; see for instance Kelly et al. 2018). Among these, hot blue stars can have luminosities exceeding $10^6\,L_\odot$. Red (cooler) stars are typically less luminous. Local measurements show that the most luminous red SG stars, such as UY Scuti or Stephenson 2–18, have luminosities below $6 \times 10^5\,L_\odot$. Similar results are found in nearby galaxies (McDonald et al. 2022). This maximum observed luminosity is known as the Humphreys-Davidson (HD) limit (Humphreys 1978).

It is unclear whether brighter red stars can exist beyond this limit, but earlier work shows that they may (Chen et al. 2015;

---

[1] After submission of this paper, Yan et al. (2023) expand this number with 11 additional transients found in new JWST data in these two galaxies.

Gilkis et al. 2021). In this case they would be detectable in arcs such as that of Spock, in regions with a sufficiently high magnification. At the redshift of the Spock galaxy, the distance modulus is 42.63 mag. A very luminous star with an absolute magnitude of -10 would have an apparent magnitude $\sim$33–34 (depending on the star temperature and filter and ignoring specific color corrections). If this star is being magnified by a factor $\mu \approx 400$, its apparent brightness would increase by 6.5 mag, making it detectable in standard HST observations. A lack of detection of such very luminous stars implies that they cannot exist in the volume being amplified by these factors. Since no stars are observed in the Spock arc in several of the observations carried out by HST, one can use this fact to set an upper limit on the luminosity of the stars in that portion of the arc. During the more frequent periods when the star is not observed, it is logical to assume that the star is being magnified by the most likely value of the magnification. Meanwhile, the star is briefly being observed during relatively short periods when the star is crossing one of the microcaustics in the source plane. The main objective of this paper is to quantify the probability that a star is being observed during those short periods. However, in order to reach that point, we first need to start with deriving the mass distribution in the cluster (the macrolens model), followed by the microlens model, then characterizing the morphology and stellar properties of the Spock arc, and finally combining all of the previous steps to compute the probability that a star is detected above some established limiting magnitude and for a given filter.

The paper is organized as follows. In Sect. 2 we briefly discuss the observations carried out during the BUFFALO program as well as the ancillary Multi Unit Spectroscopic Explorer (MUSE) data used to derive the spectroscopic redshifts. The lensing constraints and data used to derive the lens model are discussed in Sect. 3. In Sect. 4, we present the lens model derived using only lensed systems with known redshifts (spectroscopic). Section 5 presents a simple application of the lens model, where we make predictions as to the number of observed lensed galaxies around the cluster at $z = 6$ and $z = 9$. Section 6 discusses the physical parameters derived for the Spock galaxy. In Sect. 7 we briefly describe the microlensing simulations that introduce modifications to the macromodel magnification. We combine all of the elements from the previous sections and explain how we computed the probability of seeing microlensing events in the Spock galaxy (our main result) in Sect. 8. Finally, Sects. 9 and 10 discuss these results and present our conclusions, respectively.

We adopted a standard flat cosmological model with $\Omega_m = 0.3$ and $h = 0.7$. At the redshift of the lens ($z = 0.396$), and for this cosmological model, 1 arcsec corresponds to 5.39 kpc, while at $z_s = 1.0054$, 1 arcsec corresponds to 8.13 kpc. Unless otherwise noted, magnitudes are given in the AB system (Oke & Gunn 1983). Common definitions used throughout the paper are the following. We use the term macromodel when we refer to the global lens model derived in Sect. 4. The main caustic and main critical curves refer to this model. We use the term micromodel for the perturbations introduced by microlenses in the lens plane, and the term microcaustics for the regions of divergent magnification in the source plane associated with these microlenses. Finally, when referring to the effective temperature of a star, we simply denote this temperature by T.

2. Observations

In this section, we briefly summarize the high-resolution HST imaging and the follow-up spectroscopy of MACS0416 that are used to develop the lens model presented in this work.
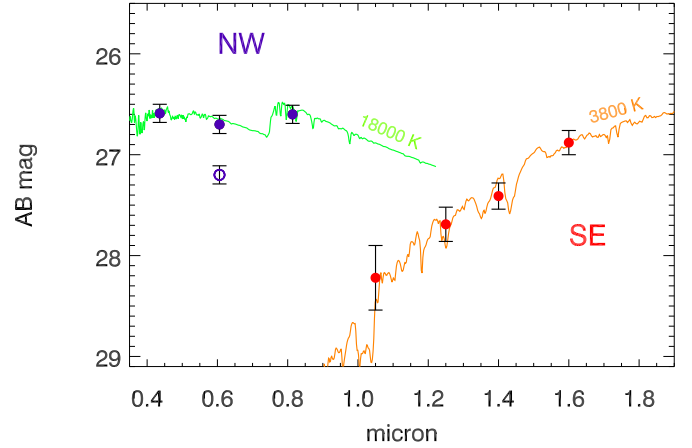
Fig. 1. Photometry of the two events (SE and NW) in the Spock galaxy reported by Rodney et al. (2018) vs. stellar models. For each event, the magnitudes in this plot correspond to the moment of maximum observed luminosity in Rodney et al. (2018) and are obtained from that work. The colored curves are synthetic models from Coelho (2014) for different star temperatures. The SE event is well described by a red SG with $T \approx 3800$ K, while the NW event is better described by a hotter star system with temperature $T \approx 18\,000$ K. Blue dots correspond to the optical bands while red dots are for the IR channels. The open circle is the magnitude measured in $F606W$ 1 day (a half day in the rest frame) before maximum. We corrected this magnitude by 0.5 mag from the relation $dm/dt \approx 1$ mag day^{-1} found in Rodney et al. (2018) where time is expressed in the rest frame of the Spock galaxy (see their Supplementary Fig. 9).

2.1. Hubble Space Telescope imaging

The first HST observations of MACS0416 were performed with WFPC2 ($F606W$/$F814W$) in 2007/2008 (GO-11103; PI H. Ebeling). These early high-resolution images of MACS0416 established this cluster as a powerful lens, leading to its selection as one of the six targets in the HFF program (Lotz et al. 2017). Thanks to the HFF program, MACS0416 is among the galaxy clusters with the deepest HST observations obtained to date. The HFF observations have been extended through the "Beyond the Ultra-deep Frontier Fields And Legacy Observations" program (BUFFALO; GO-15117; PIs C. Steinhardt & M. Jauzac, Steinhardt et al. 2020).

The BUFFALO HST mosaics include the original HFF and archival data, as described by Steinhardt et al. (2020). The mosaics are produced following the approaches described by Koekemoer et al. (2011). In Fig. 2, we show the BUFFALO color image of MACS0416. The yellow rectangle highlights the area covered by the IR filters in the original HFF program. The red rectangle shows the larger area covered in the IR bands by the BUFFALO program. Our lens model is constructed over the entire 6×6 arcmin^2 region shown in this figure.

2.2. Spectroscopy

Redshifts for both member galaxies and lensed galaxies are obtained from observations made with MUSE (Bacon et al. 2010). The MUSE observations of MACS0416 used in this work were originally presented as part of the MUSE Lensing Clusters data release (Richard et al. 2021) of 12 massive, strong-lensing clusters. Data for MACS0416 were obtained through the MUSE Guaranteed Time Observations (GTO) consortium (PID 094.A-0115, PI J. Richard) and two additional General Observation (GO) proposals (PID 094.A-0525, PI F. Bauer; PID
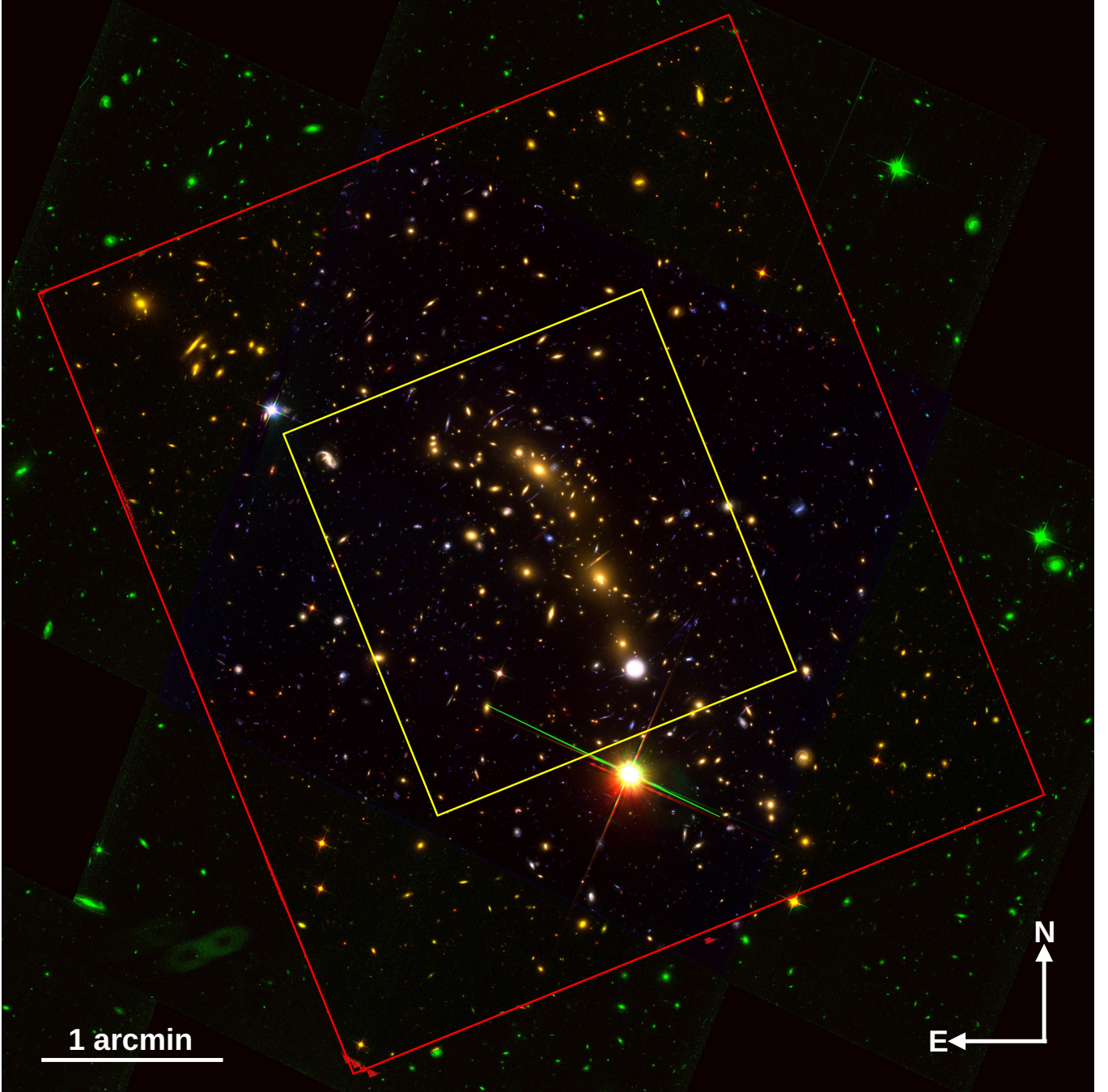
Fig. 2. BUFFALO data around the cluster. The image shown is 6 arcmin on a side. The yellow rectangle marks the region where previous IR data from the HFF program were taken. The red rectangle shows the expanded area covered by BUFFALO in the IR filters. This image corresponds to the combination of filters $F435W$, $F814W$, and $F160W$. Strong-lensing constraints are present only in the central region (yellow square) while weak-lensing constraints are spread over the entire image.

0100.A-0763, PI E. Vanzella). To maximize the observational depth, all exposures were combined into a master dataset, and for consistency each individual frame was reduced using a common pipeline. Although this procedure largely followed the standard prescription given in the MUSE Data Reduction Pipeline User Manual[2] based on the method of Weilbacher et al. (2020), some modifications were made owing to the crowded nature of cluster fields. A full description of the method and its modifications is presented in Sect. 2.5 of Richard et al. (2021) and Sect. 2.2 of Lagattuta et al. (2022). After final combination, the master

dataset has a total exposure time of 30 hr, covering an area of ~2.5 arcmin^2.

Spectroscopic candidates were identified in the field in two ways. The first method (prior targets) selected all objects in the combined multiband HST imaging using Source Extractor (Bertin & Arnouts 1996), with the size of each detected object slightly broadened (i.e., convolved with the MUSE point-spread function (PSF)) to account for resolution differences. In the second method (muselet sources), strong emission-line features were detected in the MUSE data directly, using the MUSELET routine included in the MUSE Python Data Analysis Framework (MPDAF; Piqueras et al. 2019). This allowed for a more

---

[2] https://www.eso.org/sci/software/pipelines/muse/

complete search of multiple-image systems, identifying objects that were not directly visible in the HST data alone. Regardless of the detection method used, a spectrum of each candidate was extracted using an optimally weighted (Horne 1986) algorithm. An initial redshift for each extraction was estimated using the Marz software (Hinton et al. 2016), though these were later refined by human inspection. A finalized, master list of all redshifts in the MACS0416 MUSE footprint is included in Richard et al. (2021).

3. Strong- and weak-lensing constraints

The strong- and weak-lensing catalogs have been compiled within the BUFFALO collaboration following the procedure outlined by Niemiec et al. (2023). Here we only summarize the main aspects of the process, and refer the reader to that publication for a detailed step-by-step description. The strong-lensing constraints were compiled from the existing literature (Jauzac et al. 2014; Johnson et al. 2014; Diego et al. 2015; Kawamata et al. 2016; Caminha et al. 2017; Richard et al. 2021) to produce a self-consistent and homogeneous catalog. All multiple images are revoted within the collaboration and are assigned a grade (gold, silver, or bronze) according to their reliability, with gold systems being the most reliable (spectroscopically confirmed), silver systems being less reliable (they lack spectroscopic confirmation but are good candidates based on consistency in color, morphology, and photometric redshift), and bronze being the least reliable but still potentially correct systems (as for silver systems, bronze systems lack spectroscopic confirmation and are usually unresolved, lacking morphological information). The position of each image is then visually inspected by several members of the collaboration, to ensure that the chosen positions (e.g., the emission knot, brightest pixel, etc.) are consistent within each multiple-image system. In this analysis, we only use the constraints labeled as gold to derive the lens model, which corresponds to 72 multiply lensed galaxies, resulting in 214 images when lensed by the cluster. This can be compared to the recent analysis of Bergamini et al. (2023) which used 60 individual galaxies that are multiply lensed. Two of the Bergamini et al. (2023) systems in the northeast (NE) portion of the cluster are excluded from our analysis, not because they are dubious systems, but simply because our lens models were derived before the results of Bergamini et al. (2023) were published. Adding the two Bergamini et al. (2023) systems would certainly improve our lens model, but not substantially since the region of the lens plane where these two new systems are found is already well constrained by other systems nearby. The locations of our constraints (and the new ones discovered by Bergamini et al. 2023) are shown in Fig. 3. As seen there, the new systems of Bergamini et al. (2023; marked as red circles) are not close to the Spock arc, so not adding them in our lens model has negligible impact on our main results. However, future lens models should definitely include these systems, so we add them in our curated list of constraints in the Appendix, and for the convenience of future lens modeling efforts with this cluster.

The weak-lensing (WL) catalog is produced from the reduced BUFFALO data as follows. The galaxy shapes are measured from their second- and fourth-order normalized multipole moments, using the publicly available PYRRG code (Harvey et al. 2021). All objects (background and foreground galaxies, stars), are first extracted from the mosaic images using two runs of Source Extractor (Bertin & Arnouts 1996) with different detection threshold and kernel sizes, in order to best extract both the small and large sources, with the so-called "hot/cold" method. Galaxies and stars are then separated from the image artifacts with a maximum surface brightness (μ_{max}) vs. magnitude diagram: the shape of galaxies is what carries the weak-lensing signal, while the stars are used to model the PSF and correct the measured galaxy moments. Cuts are then applied to clean the obtained galaxy-shape catalog, and (i) mask the edges and sources contaminated by the light of massive cluster members or saturated stars, (ii) remove the galaxies that are too small or too faint to have a proper shape measurement, and (iii) remove the sources with ill-measured ellipticities or errors.

The last step is to select galaxies that are located behind the lensing cluster, as foreground galaxies are not weakly lensed and would dilute the measured lensing signal. To perform this separation, we apply color–color or color–magnitude cuts, depending on the number of photometric bands available for each source. Galaxies located within both the BUFFALO ACS and WFC3 fields of view are selected in a ($m_{814W}-m_{160W}$ vs. $m_{606W}-m_{160W}$) diagram, while galaxies only covered by ACS observations in a ($m_{606W} - m_{814W}$) vs. m_{814W} diagram. The cuts are calibrated using the subsample of galaxies that have spectroscopically measured redshifts. The final background galaxy catalog contains 3235 sources. The number density of weak-lensing measurements varies across the field of view. We bin these galaxies in 1×1 arcmin^2 bins and obtain a mean surface density of 43.6 galaxies per arcmin^2 with dispersion $\sigma = 18.9$ galaxies per arcmin^2. The central region of the cluster contains no WL measurements owing to contamination from the cluster itself, but this region is well constrained by the numerous strong-lensing arcs. We consider a region of 6×6 arcmin^2, hence the number of WL constraints is 72 ($6 \times 6 = 36$ bins, each with two constraints γ_1 and γ_2).

4. The derived lens model

We use the free-form code WSLAP+ (Diego et al. 2005, 2007) to combine the WL and SL constraints from the previous section and derive the mass distribution. This code has been described in detail in earlier work, so we refer the reader to earlier references for details. A basic description, including all relevant references, is given in Appendix A. The model is available through the BUFFALO website[3].

The resulting model shows the characteristic bimodal distribution found in earlier work, with two peaks of mass centered in each of the BCG galaxies. The critical curves for $z = 1, 2, 4$, and 10 are shown in Fig. 3. The critical curves are very elongated and intersect multiple arcs at their respective redshifts. These intersection points offer unique opportunities to zoom in the highly magnified background galaxies, as discussed in more detail in Sect. 6.

Regarding the mass profile, we find that the two main clumps of mass are very similar to each other in terms of density profiles. These are shown in Fig. 4. We compute one profile centered in the NE BCG galaxy and a second profile centered in the southwest (SW) BCG galaxy. The profiles represent the projected mass along the line of sight in a cylindrical aperture. The most remarkable difference between the two profiles is that the SW BCG is more massive within the central kpc, but beyond a few kpc both profiles are very similar. We fit a generic Navarro-Frenk-White profile (gNFW), finding a reasonable fit for a model with parameters $\gamma = 0.5$, $\alpha = 2.5$, $\beta = 3$, and scale radius $r_s = 80$ kpc, where γ, α, and β are the slopes of the density in

---

[3] https://buffalo.ipac.caltech.edu/
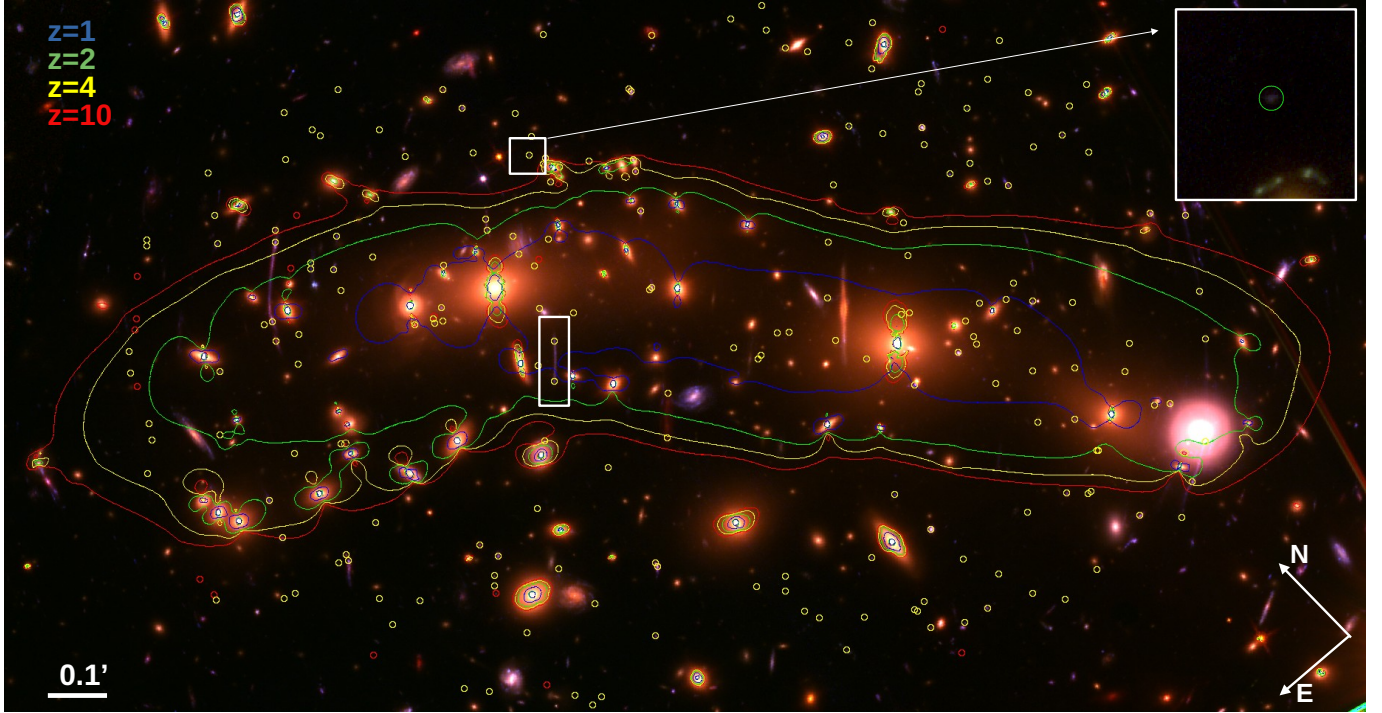
Fig. 3. Central region with arc positions. Yellow circles are the 72 systems identified in BUFFALO data and with spectroscopic redshifts. Red circles are systems not included in the previous sample but listed by Bergamini et al. (2023). The critical curves for different redshifts are shown (z = 1, 2, 4, and 10; blue, green, yellow, and red, respectively). This image is a composite made with the seven HST filters (*F*435*W*, *F*606*W*, *F*814*W*, *F*105*W*, *F*125*W*, *F*140*W*, and *F*160*W*). The white rectangle marks the position of the Spock arc. The small white square marks the position of the third counterimage of the Spock arc. A zoomed-in version is shown at top right, where the counterimage is contained within the yellow circle. The radius of this circles is 0.25″.

the innermost, intermediate, and outermost regions of the cluster, respectively (see Nagai et al. 2007, for a description of this model). The fit is done centering on each halo so it does not account for superposition effects of one halo over the other. This profile fails at reproducing the inner ~20 kpc region, but this is where baryons are expected to cool more efficiently than dark matter and form a baryonic cusp. At larger radii, our lens model benefits from the addition of weak-lensing data that extends the range of constraints up to the boundaries of the field of view shown in Fig. 2.

In terms of integrated mass as a function of radius, we show the cumulative mass profile in the inset of the same figure. The blue and red curves are again for the NE and SW clumps, while the dashed line is for the gNFW profile. In this plot we add a fourth curve (black solid line) that corresponds to a third profile centered in the middle point between the two BCG galaxies (the separation between these galaxies is ~40″). We find that the total mass contained within 1 Mpc for the black continuous line is $4.9 \times 10^{14}\,M_\odot$. Bergamini et al. (2023) derive a parametric model of this cluster and show how the integrated mass for each halo is also very similar to each other. In Fig. 4, we show a direct comparison of the profiles (centered in each halo) for our model and theirs. The models agree well in the intermediate region (30–200 kpc) where strong lensing constraints are available. Our model traces the light in the very central region while the model of Bergamini et al. (2023) is steeper. The opposite trend is found in the outskirts of the cluster. Both regimes are unconstrained by strong-lensing data, so it is natural to see the largest deviations in the innermost and outermost regions of the cluster. Quantitatively, from their Fig. 7, they demonstrate how the integrated cylindrical mass around each halo, measured at a radius of 93 kpc, is ~$4.8 \times 10^{13}\,M_\odot$. For the same

radius, we find masses $5.6 \times 10^{13}\,M_\odot$ and $5.2 \times 10^{13}\,M_\odot$ for the NE and SW halos (respectively), which is 5%–10% higher. At larger radii, Bergamini et al. (2023) find a mass for each halo of ~$3.4 \times 10^{14}\,M_\odot$ at $R = 400$ kpc. At this distance we find $3.6 \times 10^{14}\,M_\odot$ for each, the NE and SW halos.

5. Expected number of multiply lensed galaxies at high redshift in JWST images

In this section, we estimate the expected number of lensed galaxies observed at $z = 6$ and $z = 9$, based on the magnification prediction from the lens model. For sources at $z = 6$ the corresponding curve $A(>\mu)$ is almost identical to that shown in Fig. 5, with the amplitude of this curve being just ~14% smaller than the curve for $z = 9$ (based on the scaling with z of the lensing strength factor, Eq. (2.4) in Seitz & Schneider 1997). Here we consider only the case of multiple images, which takes place when the total magnification is above $\mu \approx 3$. Outside the caustic region the total magnification is below 2.5, so this assumption is well justified.

At a given redshift, the number of lensed galaxies can be expressed in the form

$$\frac{\mathrm{d}N}{\mathrm{d}\mu\,\mathrm{d}M_{\mathrm{UV}}} = \Phi(z, \tilde{M}_{\mathrm{UV}}) * \mathrm{d}V(z) N_{\mathrm{ci}} \frac{\mathrm{d}A}{\mathrm{d}\mu}, \qquad (1)$$

where M_{UV} is the absolute UV luminosity of the galaxy and $\tilde{M}_{\mathrm{UV}} = M_{\mathrm{UV}} - 2.5\log_{10}(\mu)$ is the magnitude before magnification. $\Phi(z, M_{\mathrm{UV}})$ is the luminosity function at redshift z (expressed in the usual units of number per magnitude per Mpc^3), and $\mathrm{d}A/\mathrm{d}\mu$ is the area in the source plane (expressed in arcseconds squared) with total magnification $(\mu - 0.5) < \mu < (\mu + 0.5)$. Since
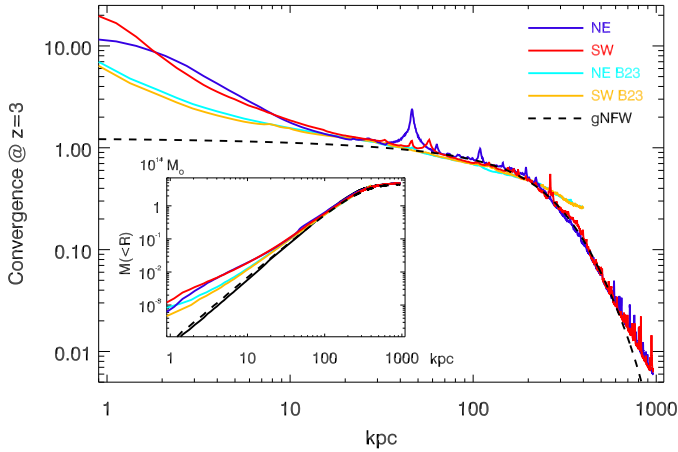
Fig. 4. Mass profile of the lens model. The blue and red solid curves show the profiles when adopting the NE and SW BCGs as central points, respectively. The mass profiles are given in dimensionless κ units assuming a source at $z = 3$. The dashed line is a gNFW profile with parameters $\gamma = 0.5$, $\alpha = 2.5$, $\beta = 3$, and scale radius $r_s = 80$ kpc. The inset shows the integrated mass as a function of radius in units of $10^{14}\,M_\odot$, and for the same three profiles shown in the larger plot. The black dashed line is the integrated profile when the center is chosen as the middle point between the two BCG galaxies (RA = $4^h16^m08.428^s$, Dec = $-24°04'21.0''$). For comparison, we show as light blue and orange the profiles from Bergamini et al. (2023).
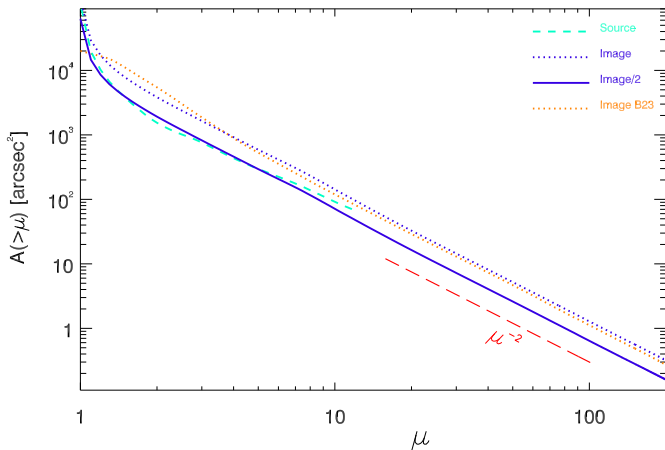
Fig. 5. Area above magnification μ at $z = 9$. The dashed line is computed in the source plane from the caustic map. The dotted line is the area computed in the image plane from the magnification map corrected by the factor μ. The solid line is similar to the dotted line but divided by a factor of 2 (in order to account for the contribution from the double image at large magnification factors). At large magnification factors, the solid curve falls as the expected μ^{-2} power law. For comparison, we show as an orange dotted line the same lensing probability for the model of Bergamini et al. (2023) at $z = 9$.

the area $dA/d\mu$ is given in arcsec^2, the volume $dV(z)$ corresponds to the volume within 1 arcsec^2 and $(z - 0.5) < z < (z + 0.5)$. The chosen binning in redshift is arbitrary. Smaller values of δz provide more accurate results, but for our purposes a redshift binning of $\delta z = 1$ will suffice. Finally, N_{ci} is the number of detectable counterimages produced by each lensed galaxy. We make the simple approximation that the total magnification μ of the galaxy is distributed into three counterimages. This is a general statement which is valid for most lensed galaxies. When the galaxy is in the central valley of the cluster caustic region, the

three counterimages have similar magnification. The central valley for MACS0416 has typical magnification $4 < \mu < 12$. Hence, we assume that galaxies falling in this central-valley region form three counterimages, each having magnification $\mu/3$. To differentiate from the valley region, we define the region with magnification $\mu > 12$ as the peak region. For typical clusters, the peak region is just a few kpc away from the caustics. For galaxies in the peak region, there are still three counterimages, but for galaxies near fold caustics (the vast majority), one of the counterimages typically has smaller magnification factors than counterimages produced in the valley region, while the other two counterimages carry most of the magnification. Hence, we do the additional approximation that galaxies located in the valley region form three detectable images ($N_{ci} = 3$), with moderate magnification factors, while galaxies in the peak region form two detectable images ($N_{ci} = 2$) with large magnification factors.

For the luminosity function of background galaxies, $\Phi(z, M_{UV})$, we follow Bowler et al. (2015) for $z = 6$ and Harikane et al. (2023), Pérez-González et al. (2023) for $z = 9$. Using these luminosity functions, we consider three different types of observations: (i) shallow, Where observations can detect galaxies brighter than $M_{UV} = -17$ mag; (ii) medium, Where galaxies with $M_{UV} = -16$ mag can be detected; and (iii) deep, reaching down to $M_{UV} = -15$ mag. These absolute magnitudes correspond to those before correcting for amplification. That is, if a galaxy is inferred to have $M_{UV} = -15$ mag, but is magnified by a factor $\mu = 10$, the magnification-corrected magnitude would be $M_{UV} = -12.5$ mag. The distance modulus for a source at $z = 6$ and $z = 9$ is 44.63 and 44.87 mag, respectively. Hence, a galaxy with $M_{UV} = -15$ mag at $z = 9$ would have an apparent magnitude (in the IR) of 29.87, within reach of deep observations made by JWST (ignoring color corrections and extinction).

The results are summarized in Fig. 6. In the larger plot, we show the number of lensed galaxies as a function of their total magnification – that is, the magnification experienced by the galaxy in the source plane. As mentioned earlier, in the image plane, each lensed galaxy usually produces between two and three detectable counterimages[4].

In our case, the transition between two and three detectable counterimages takes place when the total magnification is $\mu = 12$. This transition at $\mu = 12$ can be easily appreciated in Fig. 6, which shows the results obtained for the two redshifts ($z = 6$ and 9) and the three different depths (from bottom to top: $M_{UV} = -17$, -16, and -15 mag). As expected, most lensed galaxies have relatively small magnification factors simply because smaller magnification factors correspond to larger areas in the source plane. For the deepest observations ($M_{UV} = -15$ mag), we expect ~1 strongly lensed galaxy with total magnification $\mu \approx 30$. This is a galaxy near a caustic or even with parts of it crossing a caustic. Large magnification factors are more likely for high-redshift galaxies owing to their smaller intrinsic size. Recent results from JWST reveal very small sizes for faint galaxies at $z \approx 9$ with estimated sizes a few tens of parsecs (Williams et al. 2023). These galaxies appear unresolved even in JWST images. With tangential magnification factors of order 10, these galaxies can be resolved, so we expect that one such galaxy may be detectable in deep observations of MACS0416 with JWST. Surprisingly, from the same figure, this is the same number of galaxies we expect to observe with the same magnification factor, but at $z = 6$. This is due to the fact that the adopted

---

[4] More counterimages may appear owing to substructure or when the galaxy is also producing radial images, but this situation is not considered here.
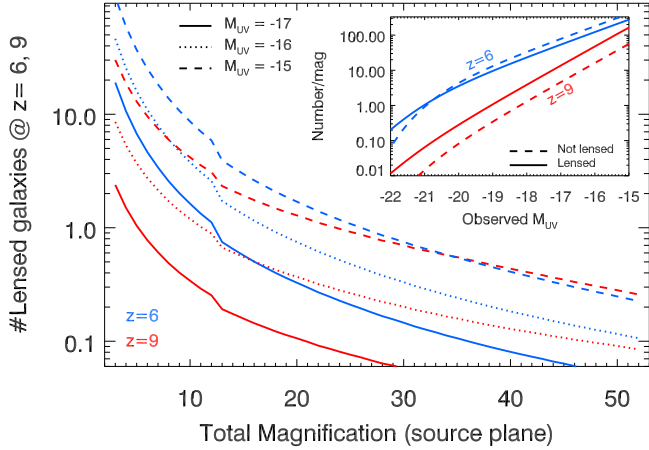
Fig. 6. Expected number of lensed galaxies in MACS0416. The larger plot shows the number of lensed galaxies behind MACS0416 at $z = 6$ (blue curves) and $z = 9$ (red curves), as a function of magnification (larger plot) or observed absolute magnitude (smaller plot). We assumed a standard luminosity function at each redshift. The different lines are for different limiting magnitudes: -17 (solid lines), -16 (dotted lines), or -15 (dashed lines). In the smaller plot the solid lines are the number of lensed galaxies for each observed magnitude, while the dashed lines are the number of galaxies one would have observed in the same magnitude bins but without lensing magnification.
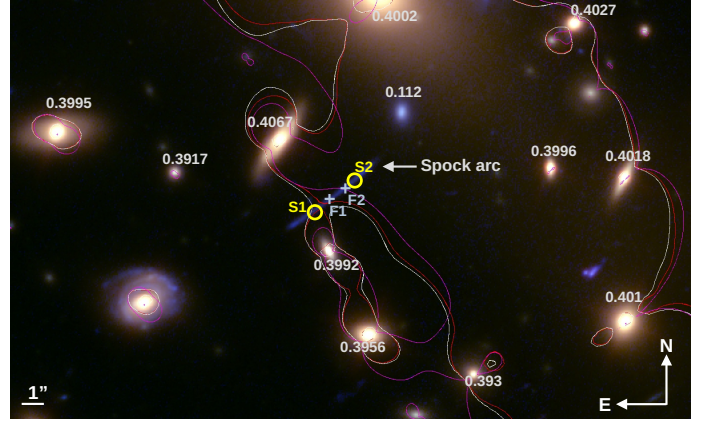

Fig. 7. Spock arc. The radial arc at $z = 1.0054$ shows the location of the two Spock transients (S1 and S2 in yellow circles) reported by Rodney et al. (2018). Two additional transients are also marked with light-blue crosses (F1 and F2). These were discovered in the same arc as part of the Flashlights program (Kelly et al. 2022). Redshifts of nearby galaxies are indicated in light gray. The white line is the critical curve at $z = 1.0054$ assuming the cluster is at $z = 0.396$. The red curve assumes the cluster is at a slightly larger redshift of 0.4 and consistent with these nearby galaxies. The magenta line is the $z_s = 1.0054$ critical curve predicted by the model of Bergamini et al. (2023).

luminosity function is steeper at $z = 9$ than at $z = 6$. This is better appreciated in the inset of Fig. 6, where we plot the number of detected galaxies (now corrected for multiplicity) as a function of the survey depth. Our model predicts that ~100 galaxies should be detectable in deep JWST observations both at $z = 6$ and $z = 9$.

In the inset of Fig. 6, we show as a dashed line the expected number of galaxies in a blank field (that is, with magnification $\mu = 1$) of similar area to the region where counterimages are expected to form in MACS0416. For galaxies at $z = 6$ we predict the classic depletion effect, where one is less likely to find faint galaxies in lensing fields than in blank fields. In this case, lensing increases the number of detections only at the bright end. However, for $z = 9$ galaxies, one is expected to be more successful (by a factor ~3) in the cluster field than in the parallel field. A similar conclusion was reached by Mahler et al. (2019) for galaxies at $z = 10$. These predictions can be tested with ongoing observations of MACS0416 that already cover the cluster region and several parallel fields. If the number density of galaxies found in the parallel fields is greater than in the cluster field, this would be a clear indication that the slope of the luminosity function must be shallower than 2 at the faint end (that is, for galaxies fainter than $M_{UV} = -15$ mag).

6. The Spock galaxy

In this section, we focus on one of the lensed galaxies behind MACS0416. Nicknamed Spock by Rodney et al. (2018), it is at relatively low redshift ($z = 1.0054$), but crosses one of the fold caustics of the cluster and hence is being significantly stretched and amplified. Relevant for the main results of this work are its size and geometry, relative position in relation to the main caustic, and stellar population derived from spectral energy distribution (SED) fitting. (These parameters and variables are all discussed in this section.)

The elongated arc from the Spock galaxy is shown in the center of Fig. 7. The lensed image forms a long arc perpendicu-

lar to the main axis and the critical curve of the cluster. A third image (with a much smaller magnification $\mu \approx 3.5$ and shown in the upper-right corner of Fig. 3) is found in the northern part of the cluster (and outside the field of view shown in Fig. 7). The elongated arc is in fact a merging image showing only a small portion of the Spock galaxy. Several lens models are presented by Rodney et al. (2018) showing how this merged image is the superposition of at least two counterimages, but possibly more than two.

The existence of the transients S1 and S2 (labeled in the image and originally reported by Rodney et al. 2018) supports the existence of multiple caustic crossings. This is further supported by the discovery of two new transients by Kelly et al. (2022) as part of the Flashlights program (and marked F1 and F2 in the figure) near the position of the two original transients. Kelly et al. (2022) suggest that S1–F1 form an image pair of the same star, while S2–F2 form a different pair of another star. This would imply that one critical curve must pass through S1–F1 and a second one through S2–F2, making the arc a superposition of at least three counterimages. The critical curve at $z = 1.0054$ from our new lens model is shown in white in Fig. 7. As expected, this critical curve intersects the arc, but it does so only once, and very close to the point between S1 and F1. The points S2 and F2 do not have a critical curve passing through them, but they are $<1''$ away from one. Small changes in the mass of the nearby member galaxies, an invisible millilens (for instance, a dwarf galaxy in the cluster), or the large-scale mass distribution, can modify this portion of the critical curve by a small amount, making a second crossing through S2–F2 possible. We show in red an alternative lens model where the redshift of the cluster is increased slightly from the originally adopted $z = 0.396$ to $z = 0.4$. The increase in redshift in this portion of the lens plane is motivated by the existence of member galaxies nearby at redshifts close to (or even larger than) $z = 0.4$, including the BCG to the north which is also slightly above $z = 0.4$. Interestingly, this alternative model places the critical curve closer to S2–F2, making the hypothesis of a second caustic crossing more plausible. Yet another alternative model is shown as a magenta curve, corresponding to the
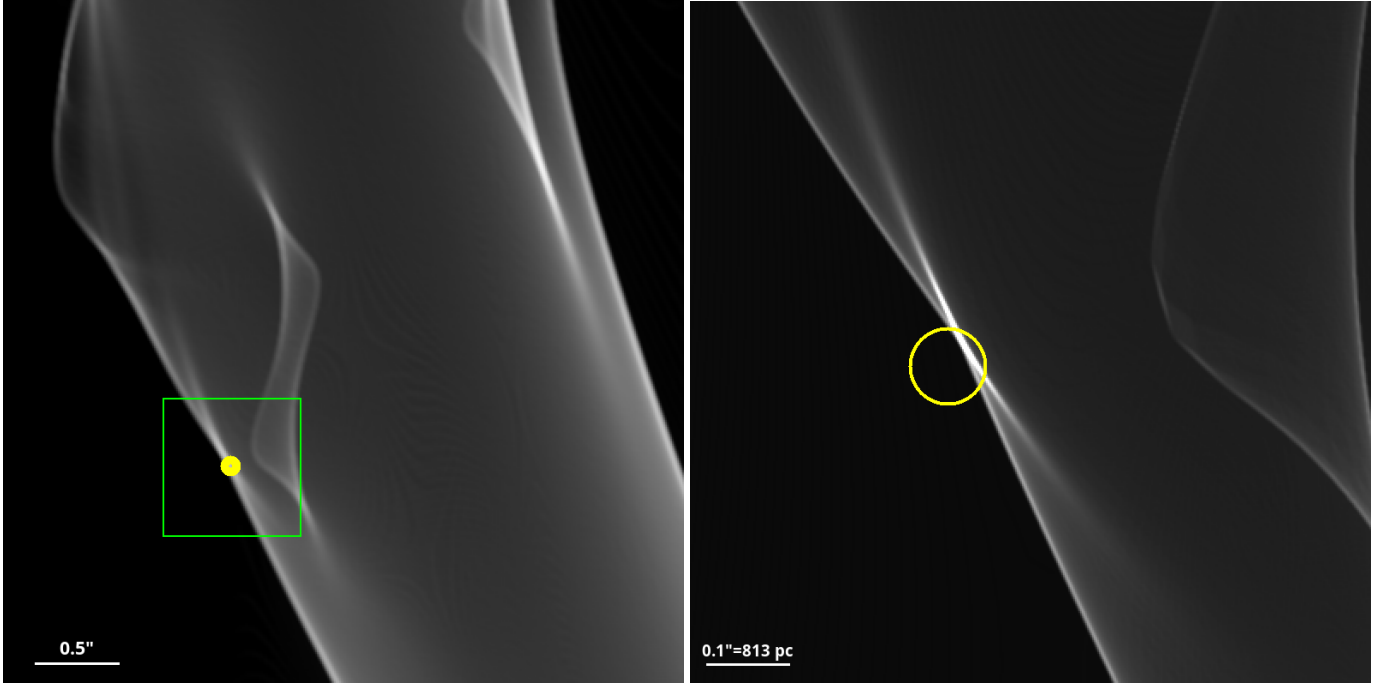
Fig. 8. Portion of the caustic region with the magnification shown as gray scale. Left: small region of $4'' \times 4''$ showing the caustics for a source at $z = 1.0054$. The yellow circle marks the predicted position of the Spock galaxy in relation to the caustics. The green square marks the region that is enlarged in the right panel. Right: zoom-in of a small portion in the caustics obtained after interpolating the deflection field to a resolution of 2 milliarcseconds per pixel and applying the inverse ray shooting method. The yellow circle represents the approximate circular shape of the Spock galaxy and its position in relation to the caustic. The length of the caustic that intersects the galaxy is estimated to be $\sim$530 pc. At a distance d pc from the caustic, the magnification in the interior region of the caustic drops as $\mu \approx 270/\sqrt{d\,(\mathrm{pc})}$.

model from Bergamini et al. (2023) at $z_{\rm s} = 1.0054$[5]. The three models show in general good agreement, but also make it obvious that a relatively large degree of uncertainty exists for the precise location of the critical curve around the position of this arc, and at this redshift.

The magnification seen by the Spock galaxy is better shown in the source plane. From the lens model we derive a map of the magnification in the source plane around the predicted position of the Spock galaxy. At the redshift of this galaxy, $1'' = 8.13$ kpc. In order to increase the spatial resolution, we interpolate the smooth deflection field before applying a standard inverse ray shooting algorithm to compute the caustics. The interpolated region is sufficiently large to guarantee that the inverse ray shooting method is not missing pixels in the image plane that land near the predicted position of the Spock galaxy. The resulting caustics are shown in Fig. 8. From this result we find that the Spock galaxy crosses a caustic, as expected from the fact that two of its counterimages form a merging pair of images. When zooming in around the Spock galaxy, we find that several caustics converge in this region. This explains the unusually large elongation of the main arc, despite the small intrinsic size of the galaxy. In the caustic map it is also evident that small changes in the lens configuration can result in multiple caustic crossings for a source placed in the right position. The magnification at the position of Spock scales as $\mu \approx 3/\sqrt{d}$, where d is the distance to the caustic expressed in arcseconds, or $\mu \approx 270/\sqrt{d}$ when d is expressed in parsecs. Using this scaling, we can estimate (later in this work) the magnification at different distances from the caustic.

6.1. Luminosity and intrinsic size of Spock galaxy

The third image of the Spock galaxy has an apparent AB magnitude of 26.6 in the $F110W$ filter. When demagnified by a factor 3.5 this corresponds to an AB magnitude of 27.96. Since the galaxy is at $z = 1.0054$, the $F110W$ filter corresponds to the visible part of the spectrum.

To obtain a constraint on the intrinsic size of the galaxy, we use this third image, which has a much lower magnification of $\mu = 3.5$. Unlike the elongated arc which shows only a portion of the source galaxy, the third image includes the full extent of the galaxy so it gives us the full picture of the demagnified source. At the position of the third image we obtain for the tangential and radial components of the magnification $\mu_{\rm t} = 2.2$ and $\mu_{\rm r} = 1.6$, respectively. The third image can be described, to first order, as an ellipse with semimajor axis $a \approx 0.2''$ and $b \approx 0.14''$. When demagnified into the source plane this corresponds to an almost circular shape with radius $r \approx 360$ pc.

Now we derive a separate constraint on the portion of the galaxy that is multiply imaged, but using the elongated arc instead, which contains only a portion of the Spock galaxy. By matching the magnification predicted by the caustics with the magnification of the arc observed in the image plane at the two extremes of the longest arc ($\mu \approx 14$ at each end and half the total magnification when one considers a double pair of counterimages), and using the scaling law for the total magnification, $\mu = 270/\sqrt{d\,(\mathrm{pc})}$, we find that the edge of the Spock galaxy must be $\sim$100 pc away from the caustic. The right panel of Fig. 8 shows our best possible interpretation of the geometry of the source in the caustic region. As noted above, a significant portion of the galaxy must remain outside the high-magnification region in order to not be multiply lensed. Only the small portion inside the caustic region gets imaged into the elongated arc. For

---

our discussion, the most interesting constraint is the length of the caustic that intersects the Spock galaxy, which we estimate as ~530 pc (see right panel of Fig. 8).

6.2. Luminosity of lensed stars

After deriving the size of the source and how the magnification scales with distance to the caustic, we can now estimate the probability of observing microlensing events, similar to the two events of Rodney et al. (2018) and the two events of Kelly et al. (2022). First, we focus on S1 and F1, which are expected to have the largest magnifications from our lens model. In what follows, we assume that S1 and F1 are two different stars, but it is also possible that they are the same star with the critical curve passing through the midpoint between them. This distinction will not have a significant impact in the discussion below. Since the stars allegedly responsible for these events are only observed during short microlensing events, lasting days to weeks, they must fall below the detection limit when only the macromodel magnification is magnifying these stars. For the two lens models shown in Fig. 7, the predicted magnification (without microlensing) is at least 350 for S1 and 180 for F1.

For the time being, let us adopt a fiducial value $\mu = 270$ for the macromodel magnification of each star, and assume F1 is a counterimage of S1; other values of μ are discussed later. Based on the scaling for the magnification, this corresponds to a distance of 0.25 pc from the caustic (the total magnification is 540, which corresponds to a separation of 0.25 pc from the caustic). If the magnification at each of the two positions is 270, the star must be fainter than AB magnitude 34.6, such that in the absence of a microlensing boost in the magnification, the star remains undetected below the threshold of 28.5 mag for a point source in the HFF. This constraint is easily satisfied by the vast majority of stars at $z = 1.0054$. During a microlensing event, these stars can get a momentary boost of ~1–3 mag (e.g., Kelly et al. 2018; Diego et al. 2018; Venumadhav et al. 2017; Meena et al. 2022), making stars as faint as AB magnitude 37 at $z = 1$ detectable. The distance modulus at this redshift is 42.63 mag, hence the star needs to be fainter than absolute magnitude -8 in order to remain undetected without the aid of microlensing (ignoring specific K-corrections, that we address in more detail below). Absolute magnitude $M_{\rm B} = -8$ is the realm of bright SG and especially hypergiant stars that can approach absolute magnitudes $M_{\rm V} \approx -10$ (Humphreys 1978). Then, the star responsible for S1 and F1 is unlikely a hypergiant, since otherwise it would be detectable at all times in the Spock galaxy, even without the occasional microlensing boost. More specifically, the star needs to have bolometric luminosity $L < 3 \times 10^7\, L_\odot$ to remain undetected in the $F814W$ filter, or $L < 1.2 \times 10^7\, L_\odot$ to be undetected in the $F200LP$ Flashlights observations. On the other hand, since microlensing can only boost the observed flux by 1–3 mag, the stars cannot be fainter than absolute magnitude $M_{\rm V} \approx -5$; otherwise, they would be undetectable even with microlensing. Stars with this luminosity are in the red and blue SG class, so this is possibly our best candidate for S1 (and F1). SG stars can have a wide range of temperatures, but can reach luminosities between ~$10^4\, L_\odot$ and ~$10^5\, L_\odot$.

Similar arguments can be followed for S2 and F2, except for this case the magnification from our lens model is almost an order of magnitude smaller ($\mu \approx 40$). Hence, without a second caustic crossing through S2–F2, and assuming S2 is a counterimage of F2, the star responsible for these two events must be 2 mag brighter, having absolute magnitude $M_{\rm V} \approx -7$. This type of star is very rare, making this possibility less likely than a sec-

ond caustic crossing between S2 and F2 that would increase the magnification and consequently lower the required luminosity of the background star.

For the remainder of this work, we assume that the stars detected in the Spock arc are SGs, with temperatures ranging from $T \approx 3500\,$K to $T \approx 30\,000\,$K. This is in good agreement with the photometry observed for S1 and S2, and shown in Fig. 1. For the cooler red SG stars, and according to the Stefan Boltzmann law, the lower temperature is compensated by their much larger radius in such a way that $L \propto R^2 T^4$ can remain very high and relatively uniform. The hotter stars are smaller in radius, but emit significantly more energy at the shortest wavelengths. Related to the wide range of possible temperatures, we need to also consider the detection band, since stars at $z \approx 1$ with $T \approx 3500\,$K will have their peak emission in the IR bands (assuming a blackbody spectrum and Wien's law), while a hot (mostly B-type) SG at the same redshift with $T \approx 30\,000\,$K will peak in the UV part of the spectrum. We then consider two HST filters, $F814W$ in the near-IR (used for the detection of the original Spock events S1 and S2) and the bluer $F200LP$ (used in the Flashlights program to detect F1 and F2). $F814W$ is well suited for stars showing a strong Balmer break ($10\,000\,$K $< T < 20\,000\,$K), while $F200LP$ is better suited for hotter stars ($T > 20\,000\,$K).

To compute the apparent magnitudes of the lensed stars in these filters, we need to adopt a model for their spectrum, f_λ. We assume the spectrum of these stars is well described (to first order) by a blackbody model with temperature T. We are hence ignoring spectral features such as absorption or emission lines, as well as discontinuities such as the Balmer break, but this simple approximation will still produce reasonable predictions. Setting the detection limit in the band to a given magnitude, $m_{\rm min}$, we can, for a given temperature, compute the minimum luminosity for a star at redshift $z = 1.0054$,

$$L_{\rm min} = \frac{L_f}{10^{0.4\Delta_{\rm AB}}}, \tag{2}$$

where $\Delta_{\rm AB} = m_{\rm min} - m_f$ and m_f is the apparent magnitude of a star at redshift $z = 1.0054$ in the chosen filter and with a fiducial bolometric luminosity L_f (that without loss of generality we fix to $L_f = 10^7\, L_\odot$):

$$m_f = -2.5 \log_{10}(F_f) - 48.6, \tag{3}$$

with F_f the usual flux received in the chosen filter and corrected by the filter response (and redshift dependence),

$$F_f(\nu) = (1+z) \frac{\int f_f(\frac{\lambda}{1+z}) S(\lambda) \lambda \mathrm{d}\lambda}{\int S(\lambda)(c/\lambda)\mathrm{d}\lambda}, \tag{4}$$

where $f_f(\lambda)$ is the flux density and $S(\lambda)$ is the filter and detector response (Bessell & Murphy 2012). The multiplicative factor $(1+z)$ accounts for the redshift correction to the flux density. This flux is given simply by

$$f_f(\lambda) = \frac{L_f}{4\pi D_l(z)^2} \frac{BB(\lambda, T)}{\int BB(\lambda, T)\mathrm{d}\lambda}, \tag{5}$$

where $D_l(z)$ is the luminosity distance and $BB(\lambda, T)$ is the blackbody spectrum for temperature T. Hence, the value of $L_{\rm min}$ represents the bolometric luminosity of the star (after accounting for magnification) needed to match the chosen magnitude limit, so stars with bolometric luminosity L and amplified by a factor μ are not detected if $(\mu \times L) < L_{\rm min}$.

Next, we need to find the maximum possible luminosity in the portion of the Spock galaxy that is being lensed. For this, we can use the fact that during the majority of the observations of the Spock arc, we observe no lensed star. We interpret this as the star being magnified by the most likely value during these observations, which is given by the mode of the curves shown in the left panel of Fig. 10. If a star is not observed when magnified by the mode, $\tilde{\mu}$, then its flux must be smaller than

$$L_{\max} = 1.3 \frac{L_{\min}}{\tilde{\mu}}. \qquad (6)$$

The factor 1.3 in the above expression is to account for the possibility that the star can also have magnifications 30% smaller than the mode. Setting this value to 1 has a small impact on our results, but we adopt the value of 1.3 as conservative. If $L_{\min}$ were interpreted as the minimum bolometric luminosity (after accounting for magnification) that a star has to have in order to be detected, $L_{\max}$ must be interpreted as the maximum luminosity (before accounting for magnification) that a star can have so it is not observed during the majority of the observations. The two constraints can be combined into the final condition for the bolometric luminosity, L, of the lensed stars:

$$\frac{L_{\min}}{\mu} < L < L_{\max} = 1.3 \frac{L_{\min}}{\tilde{\mu}}. \qquad (7)$$

Finally, we relate the bolometric luminosity with the mass of the star and the mass of the star with the IMF of the stellar population in the Spock galaxy. For the mass–luminosity relation (M–L) of main-sequence (MS) stars, we follow Duric (2004) with a steep M–L for the least massive stars and an Eddington-limit type of M–L relation for stars more massive than 55 $M_\odot$:

$$\frac{L}{L_\odot} = A \left(\frac{M}{M_\odot} \right)^\beta, \qquad (8)$$

where $A = (0.23, 1.0, 1.4, \text{and } 3.2) \times 10^4$ for the mass intervals $M < 0.43\,M_\odot, 0.43\,M_\odot < M < 2\,M_\odot, 2\,M_\odot < M < 55\,M_\odot$, and $55\,M_\odot < M$ (respectively), and $\beta = 2.3, 4, 3.5, \text{and } 1$ (respectively) for the same mass intervals. In this work, and since we require intrinsically high luminosities, only masses above $\sim 20\,M_\odot$ are relevant for our calculations. This relation between mass and luminosity is valid for stars on the MS. Red giants and SGs or white dwarfs do not follow this relation. White dwarfs are not relevant for our study, but red giants and SGs are. In order to relate masses with the IMF, we make the simplification that the abundance of red SGs is comparable to the abundance of hotter stars with similar luminosity. That is, given a luminosity, we derive the mass from the above relation, and from that mass we derive the abundance of stars with that mass. Finally, we assume that stars with this mass can have a range of temperatures where the only parameter is the slope (δ) of the distribution (related to the blue SG to red SG ratio, or simply B/R ratio):

$$dN/dT \propto T^\delta. \qquad (9)$$

Ideally, we would instead use a luminosity function for the red SGs, but this is uncertain and dependent on variables such as mass loss or binarity (Neugent et al. 2020b; Massey et al. 2023). In the expression above, $\delta = 0$ corresponds to a uniform mix of red and blue SG stars as a function of temperature. A value $\delta = -1$ results in ~ 10 times more red SGs than blue SGs, and consistent with some local measurements, while $\delta = 1$ would be more representative of a very young population of luminous
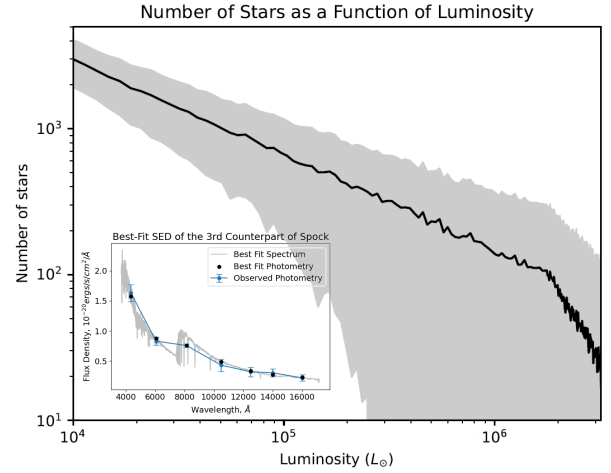
Fig. 9. Stellar luminosity function inferred from the SED fitting featured in the lower-left corner. We adopt as a fiducial model the one corresponding to the black curve in the large plot.

stars. As described below, our results depend mostly on a relatively narrow range of stars with luminosities close to (but below) the HD limit, and through the exponent δ in Eq. (9) we can control the relative abundances of blue and red SGs.

As a simple parameterization, we model the HD limit as a function of mass and temperature and then connect the mass to the luminosity through Eq. (8). In particular, we define the HD limit equivalent mass as $M_{\rm HD} = 40 + T/2500$. With this relation and for $T = 3500$ K the corresponding luminosity would be $L_{\rm HD} = 6.4 \times 10^5\,L_\odot$, while for $T = 30\,000$ K we get $L_{\rm HD} = 1.2 \times 10^6\,L_\odot$. This dependence of the maximum luminosity on the temperature of the SG star is roughly consistent with the loci defined by the observations of nearby galaxies Humphreys (1983), Davies et al. (2018), McDonald et al. (2022).

Hence, the relevant variables for us are the HD limit, given by the approximation above, and the relative ratio of blue SG and red SG stars, B/R, which for simplicity we also parameterize as a function of temperature with Eq. (9). The net number of stars with luminosity L is then given by the number of stars with the corresponding mass M, according to the M–L relation above and as predicted by the IMF. This is the strongest assumption in our model, but one that is easily rescalable (our results can be rescaled by just varying the number of SG stars in the Spock arc and controlling the B/R ratio with the parameter δ). This simplification avoids the complexity of modeling an evolved population of intermediate-mass stars (such as red SGs) and reduces the number of free parameters in the model such as age, star rotation, and especially metallicity (Langer & Maeder 1995; Wagle et al. 2020), substituting these parameters with one single degree of freedom (δ). For simplicity, we begin by presenting results with $\delta = 0$, which is close to the B/R supergiant ratio found for some mass range and age (Schaller et al. 1992; Ekström et al. 2012). The range $-1 < \delta < 1$ reproduces well the B/R ratio found in nearby young open clusters and galaxies, especially in their outskirts (Eggenberger et al. 2002; Dohm-Palmer & Skillman 2002), as in the case of the Spock galaxy where only the outer region of the galaxy is being multiply lensed. We discuss these alternative scenarios with varying δ values in Sect. 9. Our next step is to discuss how many of these luminous stars we expect in the small section of the Spock galaxy that is only parsecs away from the caustic.

6.3. Abundance of giant stars near the caustic in the Spock galaxy

We use the length of the Spock galaxy that intersects the caustic ($l = 530$ pc) and the scaling of magnification with distance found in a previous section, $\mu = 270/\sqrt{d\,(\mathrm{pc})}$, to compute the expected number of stars with a given magnification factor. For example, the area that is being magnified with factors greater than $\mu \approx 270$ (or twice 135) is then $\sim 530\,\mathrm{pc}^2$. We can find the number of luminous stars by fitting an IMF plus a scaling relation between mass and luminosity to the delensed AB magnitude of the Spock galaxy (27.96 in the V band after correction for magnification; see Sect. 6.1).

To study the stellar population in the Spock galaxy, we carry out annulus photometry on the third image to obtain the SED, as it is the only counterpart showing the entire Spock galaxy without any contamination. The circular aperture chosen is 3 times the PSF of HST, with an annulus of 1.5 times of aperture. The SED is then corrected by the lens-model magnification of $\mu = 3.5$.

We use Bagpipes (Carnall et al. 2018) to carry out SED fitting, adopting a single starburst with allowed nebular emission for the fit. Bagpipes returns a young stellar population without any line emission, where the age of the Spock galaxy is 67 ± 12 Myr, consistent with the blue color observed in the images. The best-fit current stellar mass is $9.1 \pm 1.2 \times 10^6\,M_\odot$ with a supersolar metallicity of $Z = 1.55\,Z_\odot$. These results, derived from photometry of the third counterimage, are consistent with those derived on the Spock arc by Rodney et al. (2018), who find a stellar mass of $13.8 \pm 4.5 \times 10^6\,M_\odot$ and age 290 ± 500 Myr.

After having the best-fit SED, we sample stellar populations following the Kroupa IMF, similar to what Bagpipes used. We find that the Spock galaxy has 2.8×10^4 stars brighter than $5 \times 10^4\,L_\odot$ (see Fig. 9). Among these, we expect ~ 36 stars in the $530\,\mathrm{pc}^2$ area considered at the beginning of this subsection, and that is magnified by factors $\mu > 270$.

For the age derived above, we should not expect very massive (O-type) stars to still be present; however, given the fact that the Spock arc is magnifying a very small fraction of the entire galaxy, it is possible that a pocket of more recent star formation in that portion of the galaxy still harbors one of these massive and very hot stars. Hence, for the remainder of this work we assume that these massive stars can still exit in this portion of the galaxy.

7. Microlensing simulations for the Spock galaxy

Spock harbors several alleged bright stars[6], some of which are close enough to the cluster caustic and can be detected individually when undergoing microlensing events. Two of these microlensing events were reported by Rodney et al. (2018) and two additional events by Kelly et al. (2022). With JWST observations of this cluster becoming public soon, revealing more details about this interesting arc, here we pay special attention to this galaxy and the bright stars in its interior.

The macromodel magnification represents only the expected value of the magnification in a given region of the source plane. In realty, the ubiquitous presence of microlenses in the image plane creates a network of microcaustics in the source plane. A new magnification pattern emerges from reshuffling the macromodel magnification, and transforming its distribution from a delta function (the macromodel value) to a broad probability dis-

tribution. Microcaustics from microlenses in the cluster can temporarily intersect a star in the background galaxy, providing an extra boost in magnification and making these stars detectable. In order to test the likelihood of detecting the star through a microlensing event, we have to calculate the probability of intersecting microcaustics.

The simulation with microlenses involves two main ingredients: (i) the macromodel, which is described by the tangential and radial magnifications (or similarly by κ and γ), and (ii) the micromodel, which is basically given by the surface mass density of microlenses (we assume a standard Salpeter IMF for the distribution of masses with a lower cutoff in mass at $0.02\,M_\odot$). For the macromodel we use the values of $\kappa = 0.691$ and $\gamma = 0.303$ obtained at the position S1 from the macromodel. The exact values of κ and γ are not relevant as long as they are representative of the values expected around this position. This results in magnification $\mu = \mu_t \mu_r = 166.7 \times 1.64 = 273.4$, which is in the range of magnifications expected for S1. To simulate different values of the magnification we simply change κ very slightly until the desired magnification is reached.

For the microlens model, we assume that the contribution from the intracluster light (ICL) to the total mass at the distance of S1 from the main BCG (~ 50 kpc) is $\sim 2\%$, or $\kappa_* = 0.01\,\kappa = 0.01382$. This number is in agreement with recent results (Montes 2022; Diego et al. 2023). However, given the bimodal morphology of MACS0416, and the possible recent merger activity, the ICL could be even higher, so one should consider the 2% contribution as a conservative limit. This possibility is reinforced by the fact that the ICL is still clearly visible in HST images at the position of S1. Since the critical surface mass density for the redshifts of the cluster and the Spock galaxy is $\Sigma_{\mathrm{crit}} = 2818\,M_\odot\,\mathrm{pc}^{-2}$, the surface mass density of microlenses corresponds to $\Sigma_* = 19.45\,M_\odot\,\mathrm{pc}^{-2}$. This estimate is in good agreement with the upper limit for the ICL derived by Rodney et al. (2018). They find $3.2\,M_\odot\,\mathrm{pc}^{-2} < \Sigma_* < 19.4\,M_\odot\,\mathrm{pc}^{-2}$ for the position of the Spock elongated arc. In this work we do not consider exotic forms of dark matter that could also act as microlenses, such as primordial black holes (PBHs). Earlier work based on microlensing of distant stars has constrained the abundance of PBHs to a small fraction ($<10\%$) of the total projected mass (Oguri et al. 2018).

We make a set of simulations varying the macromodel magnification, $\mu = \mu_T \mu_R$, and the surface mass density of microlenses. The resulting probability of magnification for each simulation is presented in Fig. 10. The left panel shows the distribution of the magnification when microlenses are present. Each curve corresponds to a different scenario where the macromodel tangential magnification μ_T (which is the one that varies most along the arc) and/or the surface mass density of microlenses is varied. In all cases, the radial magnification is fixed to $\mu_R = 1.63$. To first order, the most likely magnification is close to the macromodel value, while the width of the probability distribution scales with the effective surface mass density of microlenses, $\Sigma_{\mathrm{eff}} = \mu \Sigma_*$. This behavior was observed in earlier work (Diego 2019), and it is studied in more detail by Palencia et al. (2023). For the smaller values of the magnification, the probability scales as the expected μ^3 at larger magnifications (or μ^2 when expressed in $\log(\mu)$ intervals). For the most extreme values of the macromodel magnification, the probability resembles a log-normal, and the median of the probability falls below the macromodel value as already described in earlier work (Diego et al. 2018; Diego 2019; Palencia et al. 2023). In the right panel of Fig. 10 we show the cumulative distribution for the magnification, and for the same scenarios shown in the left panel.

---

[6] See Rodney et al. (2018) for possible alternative interpretations.
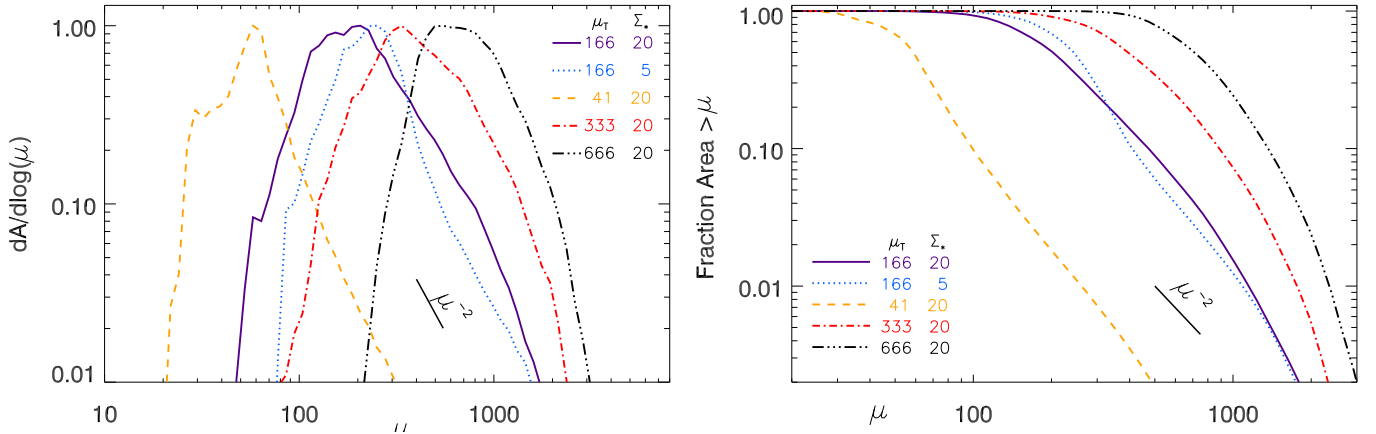
Fig. 10. Microlensing probability of magnification for the Spock galaxy. Left: relative probability of magnification in different scenarios where the macromodel tangential magnification (μ_T) or the surface mass density of microlenses (Σ_* expressed in units of $M_\odot\,\mathrm{pc}^{-2}$) is varied. In all cases, the radial component of the macromodel magnification is fixed to $\mu_\mathrm{R} = 1.63$. Different values of the tangential magnification can be interpreted as different distances to the critical curve. At the lowest magnification values considered, the probability of large magnification follows the expected μ^{-2} law. For larger values of μ_T, the probability resembles a log-normal. Right: fraction of area in the source plane with magnification factors above a certain value. The models are the same as in the left panel.

If we consider the probability of magnification to be over a factor 1000, we see from this figure that it is above $\sim 2\%$ for any star that is within 1 pc from the cluster caustic (or macromodel magnification greater than $166 \times 1.63 = 270$). Surprisingly, the case where the surface mass density of microlenses is $\Sigma_* = 5\,M_\odot\,\mathrm{pc}^{-2}$ has the same probability as the case where $\Sigma_* = 20\,M_\odot\,\mathrm{pc}^{-2}$. The probability of magnification normally scales with Σ_* (Palencia et al. 2023), so one would naively expect the case with higher Σ_* to have larger magnification. This unexpected behavior is explained by the tail of the magnification of the case with $\Sigma_* = 5\,M_\odot\,\mathrm{pc}^{-2}$, which maintains the μ^{-2} scaling longer (i.e., toward higher magnifications) than the case with $\Sigma_* = 20\,M_\odot\,\mathrm{pc}^{-2}$, that for $\mu \approx 1000$ is already falling faster than μ^{-2}, as shown in the left panel. As discussed by Palencia et al. (2023), the breaking of the scaling takes place when the effective surface mass density $\Sigma_\mathrm{eff} = \mu\Sigma_* \approx \Sigma_\mathrm{crit}$. Similar results were found in earlier work (Schechter & Wambsganss 2002; Schechter et al. 2004; Vernardos et al. 2014). For macromodel magnification $\mu = 666 \times 1.63 = 1086$, the probability of having magnification greater than $\mu = 1000$ is already 20%, but the star spends most of its time with magnification values below $\mu = 800$.

One final ingredient relevant for the discussion below is the typical timescale of a microlensing event of a distant star near a critical curve. Here we are interested in the timescale for crossing one microcaustic, much smaller than the time required to cross the entire microlens, which can span decades (Mosquera & Kochanek 2011). The duration of a high-magnification event produced by a microlens depends on the size of the source, the relative velocity between the source and the web of microcaustics (a redshift-dependent variable; Kayser et al. 1986; Kochanek 2004), the direction of motion, the mass of the microlenses, and the macromodel magnification. For the redshifts involved in this work, a typical velocity is $v = 500\,\mathrm{km\,s}^{-1}$ (Neira et al. 2020)[7]. At this velocity, the relative position between a source at $z = 1$ and the web of microcaustics changes by 0.17 nanoarcseconds per day. This is approximately equivalent to $100\,R_\odot$ at $z = 1$. During a star-caustic crossing, the magnification plateaus with a timescale that is proportional to the

radius of the lensed star (R_*) and a maximum magnification that is inversely proportional to $\sqrt{R_*}$ (Miralda-Escude 1991). That is, a star with radius $\sim 100\,R_\odot$ can cross the microcaustic in ~ 1 day, during which time it will be at its maximum possible magnification. A typical microlens near a critical curve with macromodel magnification of order 100 produces high magnification factors ($\mu > 1000$) at distances between 1 and 5 nanoarcseconds from the microcaustic (depending on the mass of the microlens and where the crossing takes place near the cusps or folds; Diego 2022). This results in timescales between ~ 1 week and ~ 1 month (both modulated by the factor $500/v$), during which luminous stars can be detected as their brightness increases by ~ 2–3 mag. This estimated timescale is consistent with alleged microlensing events such as Icarus (Kelly et al. 2018) or the two events in the Spock galaxy reported by Rodney et al. (2018). This timescale agrees also with previous estimates derived for QSO microlensing (Neira et al. 2020).

8. Probability of detecting a microlensing event in the Spock galaxy

Now we have all of the ingredients to do our final calculation and compute the expected number of stars that are detected above a given detection threshold and in a specific filter. For simplicity, we consider five regions of fixed magnification, each at a given distance from the caustic. The width of each region, Δ_pc, is determined from the scaling law $\mu = 270/\sqrt{d\,(\mathrm{pc})}$, by imposing that at the boundaries of the region the magnification changes by 30% with respect to its central value. We fix $\Sigma_* = 20\,M_\odot\,\mathrm{pc}^{-2}$ and $\mu_\mathrm{R} = 1.63$ in all regions, and vary only the tangential magnification which takes the values $\mu_\mathrm{T} = 41$, 83, 166, 333, and 666 (all shown in Fig. 10, except $\mu_\mathrm{T} = 83$, which for simplicity is omitted). Then we take the model derived from the SED fitting and compute the expected number of stars in the region of length 530 pc and width Δ_pc (this is an expected number, so it can be less than 1). Finally, all of the stars in this region are magnified by the corresponding constant magnification factor in the region (half the total magnification). We consider different stellar masses (or luminosities) and temperatures. For each combination of mass and temperature, we compute its bolometric luminosity using Eq. (8) and its apparent magnitude in the

---

[7] This velocity involves the relative transverse motion of three planes: observer, lens, and source; see Appendix B of Kayser et al. (1986).
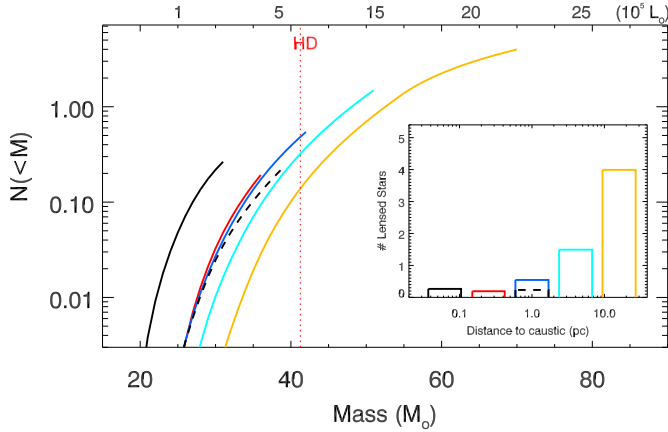
Fig. 11. Number of stars vs. distance. The large plot shows the cumulative number of stars observed at different distances from the caustic, as a function of the star mass. In this and other plots, the mass has to be interpreted as the equivalent mass of a MS star with the same luminosity. SG stars normally have smaller masses than its equivalent MS star. We assume observations reach a limiting magnitude of 28.5 in HST's $F814W$ filter. Stars from the MS with equivalent masses below $\sim20\,M_\odot$ are too faint to be detected, even at the largest magnification factors considered here. Each curve stops when $L_{\max}$ is reached. The total number of stars expected at each distance is shown in the inset at the bottom right. Each bin in the inset is centered at a given magnification (or distance to the caustic) and the width is computed from the $270/\sqrt{d\,(\mathrm{pc})}$ relation taking 30% above and 30% below the magnification of the bin. colors in the inset correspond to colors in the larger plot. In all cases except for the dashed curve, the assumed surface mass density of microlenses is $\Sigma_* = 20\,M_\odot\,\mathrm{pc}^{-2}$, and all stars are assumed to have the same temperature of $10\,000\,\mathrm{K}$. The dashed curve corresponds to separations of $\sim1\,\mathrm{pc}$ from the caustic, but for a surface mass density of microlenses of $\Sigma_* = 5\,M_\odot\,\mathrm{pc}^{-2}$. The maximum probability of seeing a lensed star is found at $\sim16\,\mathrm{pc}$ from the caustic (yellow bin), if one ignores the Humphreys-Davidson (HD) limit (vertical dotted line). If one considers this limit, the most likely distance to observe stars is at $1\,\mathrm{pc}$ (dark blue bin corresponding to total magnification $\mu \approx 270$, or $\mu = 135$ for each counterimage), in good agreement with the observations and lens model.

selected filter from Eq. (3). If the star is brighter than $m_{\min}$, then it is counted as a detection.

The result is shown in Fig. 11 for the five different regions, and for stars with temperature $T = 10\,000\,\mathrm{K}$ being observed with the HST $F814W$ filter and above limiting magnitude $m_{\min} = 28.5$ in this filter. In the larger plot, we show as solid lines the cumulative number of detected stars in each one of the five distance bins, and as a function of the mass of the star (or luminosity as shown in the top scale). The curves stop where the luminosity reaches $L_{\max}$ (see Eq. (6)). At short distances from the caustic (black curve), the macromodel magnification is so large that faint stars can be more easily detected. The black curve also assumes that the double image of the lensed star forms an unresolved source, so its flux doubles. This situation is similar to the case of "Earendel" or "Godzilla", where given the large inferred magnification factors, the double image is expected to appear as a single unresolved source (Welch et al. 2022; Diego et al. 2022). In this situation, the cumulative function grows faster for less luminous stars. On the opposite extreme, at large distances from the caustic (yellowish curve), where the macromodel magnification is smaller, only the brightest stars can be detected. These are rarer than less luminous stars, but since one is integrating over larger areas, the smaller probability of seeing these stars is partially compensated by the larger area. The prediction at

the smaller macromodel magnification values assumes stars can exist beyond the HD limit (marked by a vertical dotted line). If the HD limit still holds at this redshift, the number of stars detected in the yellow bin would drop by a factor of ~50. In a scenario where there are no stars above $L = 6 \times 10^5\,L_\odot$ for temperatures $T = 10\,000\,\mathrm{K}$, we expect the maximum probability of detecting a star at distances of $\sim1\,\mathrm{pc}$ from the caustic (dark-blue curve), or at magnification factors $\mu \approx 270/2$ (the factor 2 accounting for the double image, each carrying half the magnification), in excellent agreement with S1 and F1. Accounting for the contribution from neighboring distances, and after imposing the HD limit, we find that the expected number of lensed stars at the position of S1 and F1 is of order 1, in very good agreement with the observations.

In the same plot, we also show as a dashed line the case where the surface mass density of microlenses is reduced by a factor of four – that is, $\Sigma_* = 5\,M_\odot$. Despite having fewer microlenses, the probability of large magnification is similar to the scenario where we have four times more microlenses, as discussed earlier, resulting in a similar number of predicted lensed stars. Hence, our results are relatively insensitive to the particular choice of Σ_*, as long as it is within the constrained range.

The final number of stars in each region is the result of two competing effects. On one side, larger magnification factors make the detection of the more abundant fainter stars easier, but on the other side, regions with larger magnification factors are considerably smaller. There is a sweet spot where the combination of the two effects maximizes the probability of seeing a star. In the inset plot of Fig. 11, we show the total number of detected stars as a function of the distance to the caustic. The width of the bins in the inset corresponds to the width Δ_{pc} used in the calculation. Again, in this plot we have assumed that stars can exist beyond the HD limit. If one sets the HD limit as the maximum luminosity, the light blue and green bins would have ~5 and ~50 times fewer lensed stars, respectively. In that case, we deduce that the best chance of finding lensed stars is when the total magnification of the double image is $100 < \mu < 300$, corresponding to a physical distance of one to a few parsecs from the caustic (dark-blue ad light-blue curves, respectively). The fact that we do not observe numerous lensed stars at larger distances from the critical curve is a direct indication that the HD limit must also be applicable at this redshift.

The dependence with the mass (or luminosity) of the star is better appreciated in Fig. 12, where we show the expected number of detected stars above AB magnitude 28.5 in HST's filter $F814W$, and per mass interval. At short distances from the main caustic (large magnification factors), the fraction of stars that is detected is proportional to the adopted IMF. The black solid curve corresponds to the case with maximum magnification and assuming both counterimages of the lensed star form an unresolved pair (so the observed flux doubles, making the detection of fainter stars possible). At larger distances from the main caustic, as the magnification drops, lensed events naturally select the brightest stars. The most extreme case is given by the yellow curve (macromodel magnification $\mu \approx 67$), where the most likely stars to be detected are the most luminous ones. This dependency with the macromodel magnification offers a unique opportunity to probe the most luminous (and rare) stars in distant galaxies, since these would be the only ones visible at relatively large distances from the critical curves of powerful lenses. In the particular case of the Spock galaxy, since we do not see the predicted abundance of lensed stars at these large distances from the critical curve, we can conclude that these stars cannot exist, as discussed above.
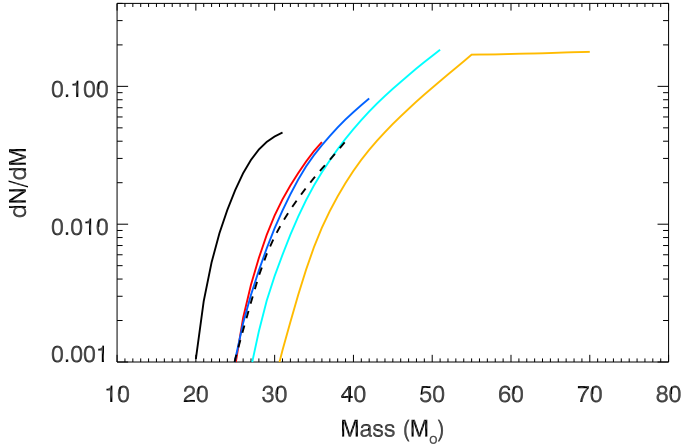
Fig. 12. Mass dependence vs. distance in HST's $F814W$ filter at depth 28.5 mag. This figure is the differential version of Fig. 11. The colors and linestyles of the curves have the same interpretation as in the previous figure (that is, yellow is for the farthest distance to the caustic and black for the closest). The dashed line again represents the case where $\Sigma_* = 5\,M_\odot\,\mathrm{pc}^{-2}$ as in Fig. 11. The plateau in the yellow curve marks the transition in the M–L relation at $M \approx 55\,M_\odot$.

Fig. 13. Same as Fig. 11 but for a shallower observation where the limiting magnitude is 27.5 ($T = 10\,000$ K). Most lensed stars are predicted at larger separations from the critical curve, but if one imposes as maximum luminosity the HD limit, lensed stars are observed mostly at the largest magnification factors – that is, closer to the caustic and critical curve.

We observe a general trend with the depth of the observation that can be appreciated when comparing the previous result with a shallower observation using the same filter, and assuming the same temperature for the lensed star, but reaching only 27.5 mag. In Fig. 13, we have allowed $L_{\max}$ to be larger than the HD limit. This explains the counterintuitive result shown, where shallower observations predict more events in the light-blue bin than in the same bin, but for the deeper observations of Fig. 11. This is due to the fact that $L_{\max}$ is larger in the shallower observation, hence the total number of lensed stars is integrated over a wider range of luminosities. That is, luminosities as high as $5 \times 10^6\,L_\odot$ are permitted in the calculation of the shallow case, but they are not permitted in the deeper case, which is better constrained and already excludes these luminosities because they are not observed at magnification factors $\mu = \tilde{\mu}$. As in the previous case, if the HD limit is adopted, the number of detections drops significantly and all bins contain <1 star; the only exception is the black curve (closest distance to the caustic), where we expect ~0.2 lensed stars. Hence, we can conclude that in shallower observations of the Spock arc, we expect to detect lensed stars at the critical curve, or very close to it, but with a relatively low probability. In particular, we expect that one in five observations at depth $F814W = 27.5$ mag may show a lensed star. But this estimate is made assuming all stars more massive than $M \approx 20\,M_\odot$ have $T = 10\,000$ K. Cooler or much hotter stars are less likely to be detected (for the same bolometric luminosity) since the peak of their emission does not fall in the $F814W$ filter; hence, this estimate needs to be corrected by the fraction of stars with $T \approx 10\,000$ K, making the detection of such stars even less likely.

In contrast, deep observations (as in Fig. 11) naturally increase the number of detections, with the bulk of them moving farther away from the critical curve. The deeper the observation, the farther one can reach down the luminosity function, and also the farther away from the critical curve one expects to see lensed stars. In this case, the larger area of smaller-magnification regions dominates over the luminosity of the brightest stars, and we predict a larger number of detections in regions where the magnification of a lensed star is $\mu \leq 150$ than in regions with larger magnification factors. For galaxies at larger redshifts, stars
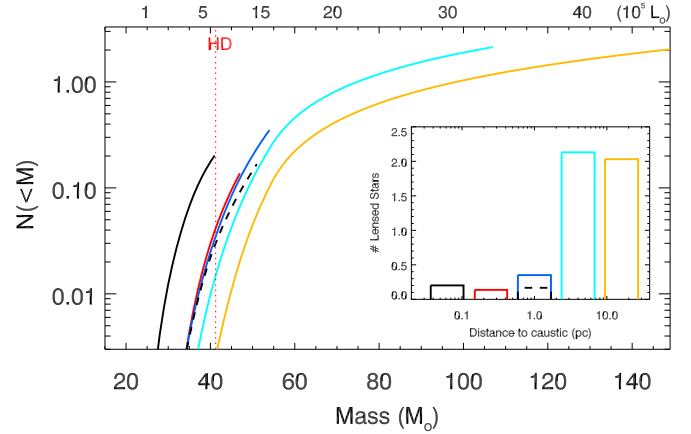
are fainter and one requires larger magnification factors, making the situation similar to the shallow observations at lower redshift discussed above.

For an even deeper observation of the Spock arc, we considered a depth of 29 mag similar to the one reached by the Flashlights program with the wide filter $F200LP$. The result is presented in Fig. 14. For easier comparison with the previous results, we required that all stars have the same temperature ($T = 10\,000$ K). This is a bluer filter that is more sensitive to hotter stars, so despite the increased depth, we observe a reduction in the expected number of lensed stars when compared with the shallower observations of $F814W$ at 28.5 AB mag depth. Ignoring events above the HD limit (at $M \approx 41\,M_\odot$), we expect about 40% fewer lensed stars with $T = 10\,000$ K in the Flashlights observation. However, as we see later, this filter performs much better for hotter stars, and for which the HD limit is also higher. The range of magnifications (or distances from the critical curve or caustic) at which we expect to see lensed stars in this filter is similar to the case of the $F814W$ filter at 28.5 mag depth. After integrating over the entire range of distances, the number of predicted stars is ~1, similar to the case of $F814W$, and in good agreement with the observations.

We conclude that in general, each arc, redshift, filter, and depth needs to be studied individually since there is no general rule that applies to all. Next we study how these results depend on the effective temperature of the star.

8.1. Dependence on star temperature

The results presented above are obtained assuming all lensed stars have the same temperature. Obviously, this is an unrealistic assumption since SG stars can have a wide range of temperatures from ~3500 K to several tens of thousands of degrees. For a given redshift and temperature of the lensed stars, there is an optimal filter for which the star is more likely to be detected. We present the expected number of detections above AB magnitude 28.5 as a function of the star temperature for the HST filter $F814W$ in Fig. 15. For this particular filter, star redshift, and depth, the most likely star to be detected has $T \approx 10\,000$ K, and as discussed above, we should expect to find these stars with magnifications in the range $100 < \mu < 300$. We emphasise again
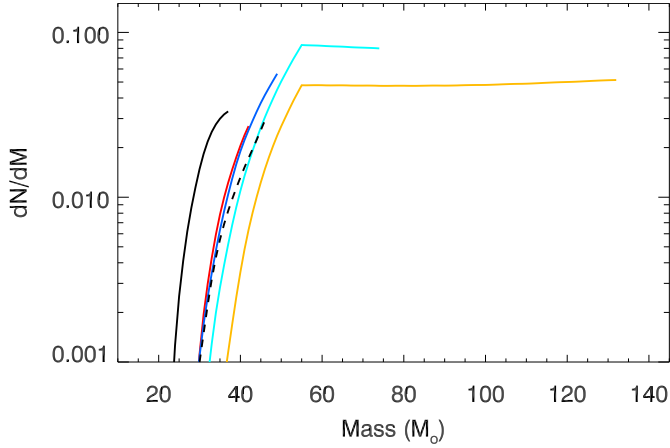
Fig. 14. Number of stars detected per mass interval as a function of distance to the critical curve (or magnification) in filter $F200LP$ at depth 29 mag (Flashlights). All stars are assumed to have the same temperature $T = 10\,000$ K. The colors and styles of the lines are the same as in previous figures (yellow for the farthest distance to the caustic and black for the closest one).
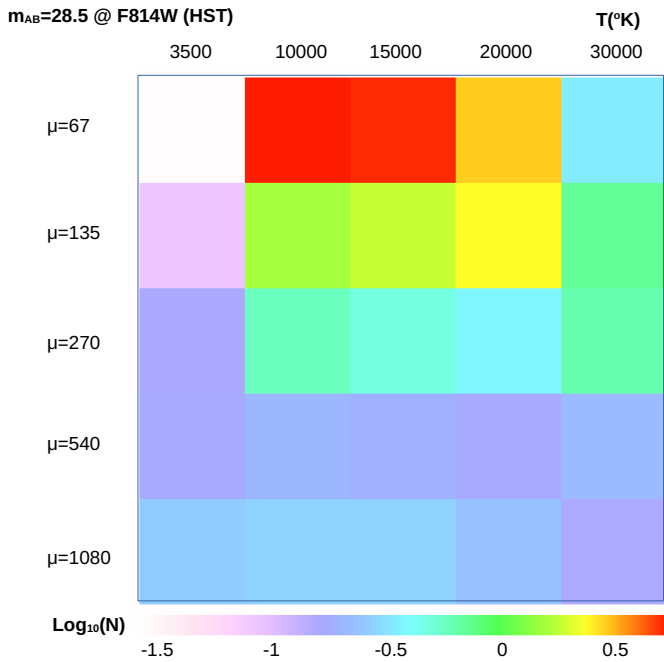
Fig. 15. Number of stars vs. star temperature and macromodel magnification (or distance to the critical curve) for HST's $F814W$ filter and at limiting AB magnitude of 28.5. For each each bin we have assumed that all lensed stars have the temperature of that bin, so one needs to correct the total number in each bin by the fraction of stars with that particular temperature.

that at the lowest magnification values considered in this figure, only stars above the HD limit can be detected, so if these stars do not exist with the abundances we have assumed, the number of stars in these bins should be considerably reduced.

Regarding the bluer $F200LP$ filter, the number of detections as a function of temperature and magnification is shown in Fig. 16). The number of lensed stars in the temperature range $10\,000\,\text{K} < T < 20\,000\,\text{K}$ is very similar to the shallower F814 = 28.5 mag observation, but we observe an increase in the predicted number of events for stars with $T > 20\,000$ K. The reduc-
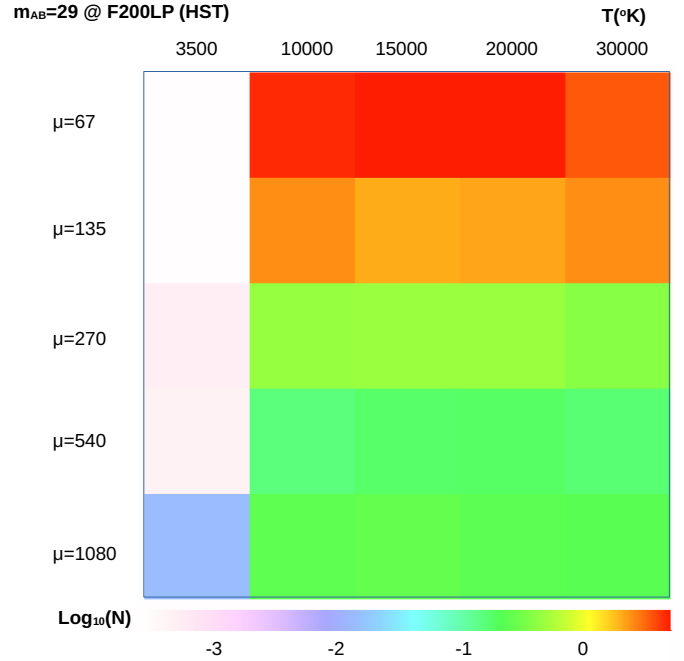
Fig. 16. Similar to Fig. 15 but for HST's $F200LP$ filter and limiting AB magnitude 29.

tion in number of events, when one considers the HD limit, is still applicable for the bins with the smallest magnification and $T < 15\,000$ K, but hotter stars can be more luminous than $6 \times 10^5\,L_\odot$. Hence, we expect to see more lensed stars in $F200LP$ at 29 AB mag depth than in $F814W$ at 28.5 mag depth. This matches well the fact that in each of the two epochs of the Flashlights program a lensed star was spotted, while the observations with $F814W$ had a smaller success rate.

When we account for all of the temperatures and possible magnifications, the expected number of detected stars is summarized in Table 1. The numbers in the columns with $\delta = 0$ represent the sum of all the numbers in Figs. 15 and 16 divided by 5, which is the number of temperature bins. This factor 5 is the fraction of stars that fall in each temperature bin when one takes $\delta = 0$ in Eq. (9). That is, we are assuming that the number of stars per temperature bin (before magnification) is homogeneous. In the table we show the case where the HD limit is imposed and when stars above this limit are allowed to exist. The numbers in the case where the HD limit is imposed are relatively consistent with the observations (as discussed later), while the numbers when the HD limit is not imposed are not consistent. Hence, our results in Table 1 clearly favor a scenario where the HD limit is still valid at $z = 1$. We also include the case of JWST observations at 2 μm and reaching 29 mag. The gain provided by JWST is obvious, providing a factor ~8 more detections. If our model is correct, in every single pointing of JWST we should observe ~5 lensed stars. Different observations will show new stars, or variations in the flux of stars observed in previous observation, or a combination of both (new stars and flux fluctuations). The high sensitivity of JWST to the most luminous red SGs at wavelengths $\lambda > 2$ μm will allow a constraint on their maximum luminosity and establish the validity of the HD limit at this redshift. The last two columns in Table 1 show the predictions for alternatives values of the B/R ratio (or δ). These are discussed in more detail in Sect. 9.

Table 1. Number of lensed stars expected with and without imposing the HD limit.

Filter	Depth	no $HD_{\delta=0}$	$HD_{\delta=0}$	$HD_{\delta=1}$	$HD_{\delta=-1}$
$F814W$	27.5	2.1	0.18	0.15	0.13
$F814W$	28.5	4.6	0.9	0.8	0.6
$F200LP$	29	5.6	1.0	1.2	0.5
$F200W$	29	17.5	4.6	1.5	10.5

Notes. Numbers represent the total of the temperature–magnification diagrams in Figs. 15, 16, and 18. The slope δ in Eq. (9) controls the relative abundance of red SGs vs. blue SGs. $F814W$ and $F200LP$ are HST filters, while $F200W$ is a JWST filter.
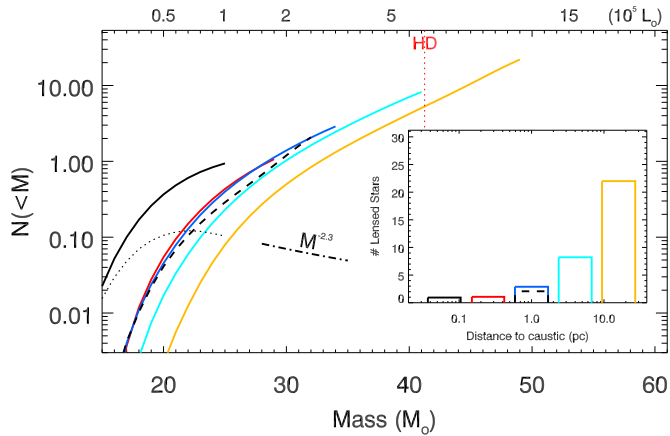

Fig. 17. Cumulative number of detected stars in JWST's $F200W$ filter, at depth 29 mag, and for stars with $T = 3500$ K. SG stars with this temperature are often less massive than implied by the abscissa. The colors and line styles are the same as in Fig. 11. The HD limit is marked by HD and a red vertical dotted line in the plot. Cool SG stars beyond the HD limit are not observed in our local universe, but if they exist in larger numbers at $z \approx 1$, JWST has the best chance to see them in regions of the Spock arc with magnification factors $\mu \approx 100$ (light-blue and yellow curves). The black dotted line represents the differential function dN/dM of the black solid curve (corresponding to the largest magnification factor, $\mu \approx 1000$), and it shows a turnover at $\sim 20\,M_{\odot}$.

8.2. Predictions for JWST

It is natural to expect the number of discovered lensed stars at cosmological distances will increase with JWST observations. Owing to its sensitivity to longer wavelengths, JWST will extend the detections to lower-temperature stars, making possible the detection of red SGs with temperatures $T \approx 3500$ K. The first such example is Quyllur, a red SG at $z = 2.1878$ setting the record for the first SG star detected by JWST beyond $z = 1$ (Diego et al. 2023). Other lensed stars have been reported by JWST in recent months (Chen et al. 2022; Mahler et al. 2023; Pascale et al. 2022; Meena et al. 2023b).

First we consider an observation at 29 AB mag depth. We also consider a cool red SG star, which is more likely to be detected in the IR by JWST. The expected number of detections with JWST in the Spock arc is shown in Fig. 17, which corresponds to the $F200W$ NIRCam filter and assumes one can detect stars above AB magnitude 29 in this filter. In this case, JWST will be detecting mostly red SGs, and preferably in lower-magnification regions. At $z \approx 1$, the peak of the emission of a star with $T = 3500$ K falls in the $F200W$ filter, so naturally this filter selects those stars at that redshift.
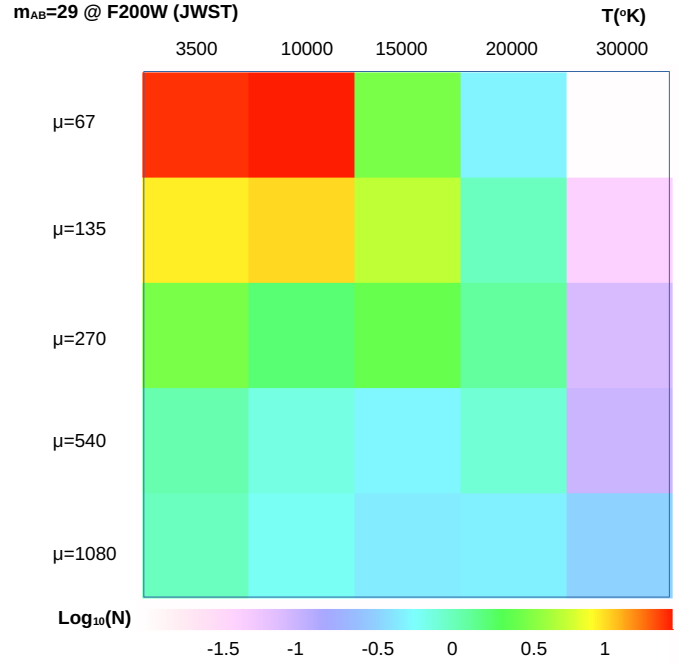
Fig. 18. Similar to Fig. 15 but for JWST's $F200W$ filter and limiting AB magnitude 29.

One interesting result from Fig. 17 is that the differential number of detections in the bin with the largest magnification (dotted black curve) starts to drop with mass following the shape of the IMF. This phenomenon takes place when the minimum magnification allowed by microlensing fluctuations times the luminosity of the star is above L_{min}. In this case, all stars more luminous than this will be detected and the number of detections traces directly the IMF. Even deeper observations with JWST will repeat the same phenomenon at larger distances from the critical curve, allowing one to probe different portions of the IMF at different separations from the critical curve. Hence, JWST will detect any red SG brighter than $\sim 10^5\,L_{\odot}$ that is closer than 0.1 pc from the caustic. This corresponds to an area of $\sim 50\,\text{pc}^2$ in the Spock galaxy; hence, a lack of detection of SGs in this regime implies a density $\rho_* < 0.02\,\text{pc}^{-2}$.

When considering the dependence with temperature, as shown in Fig. 18, we predict a substantial number of red SGs to be detected by JWST at moderate magnification factors $\mu \approx 67$. These would be spread along the Spock arc as a population of unresolved sources, and show occasional fluctuations in flux as they move across the network of microcaustics. However, as in previous cases, most of the predicted detections in this bin lie above the HD limit (see Fig. 17), so if these stars do not exist, the number of events in the reddest bins should be reduced accordingly. Lack of a significant number of detections by JWST, or relatively low numbers of red stars spread over the arc, would set a limit on the maximum luminosity of red SG stars at $z \approx 1$, similar to the HD limit established at $z \approx 0$. On the contrary, a significant number of stars detected at relatively low magnification factors would imply that red SGs can be intrinsically more luminous at $z \approx 1$ than at $z \approx 0$.

9. Discussion

In Sect. 5 we presented the expected number of lensed galaxies at $z = 6$ and $z = 9$. Recent work based on JWST on cluster fields

appear to show a deficit of galaxies beyond redshift 5 when compared with parallel or blank fields (Bhatawdekar et al., in prep.). The deficit at $z = 6$ can be easily understood as a depletion effect owing to the shallower than 2 slope of the luminosity function at the faint end. We predict that a similar depletion effect must exist for $z = 6$ galaxies multiply lensed by MACS0416. However, for $z = 9$ (and probably also for redshifts beyond this one), we predict that ∼3 times more galaxies should be found in the cluster field than in blank fields (ignoring cosmic variance). This prediction is based on recently constrained slopes for the luminosity function that find this slope to be steeper than $\alpha = 2$. If the slope is instead shallower than $\alpha = 2$, a depletion effect, similar to the one at $z = 6$, should be taking place. Simply counting $z > 9$ galaxies around clusters, and comparing with the census of similar galaxies in blank fields, is a simple way of probing the slope of the faint end of the luminosity function. The ratio $N_{\mathrm{cluster}}/N_{\mathrm{field}}$ can then be directly related to the magnification, but also to the slope α (Umetsu et al. 2015; Umetsu 2020).

Regarding the microlensing events identified in the Spock galaxy, our findings are consistent with observations only if the HD limit is still valid at $z = 1$. Assuming this limit is valid at this redshift, and accounting for different temperatures, we expect that ∼0.5 lensed stars should be detectable per pointing with HST's $F814W$ filter that reaches 28.5 mag, as shown in Table 1. Focusing on the SE event (S1) reported by Rodney et al. (2018), and on the deeper observations from their FrontierSN program, their observations cover a period of ∼30 days, with a very good cadence of ∼1 observation per day except for two blind periods of ∼3 and ∼9 days for which there are no observations. In this period one event is reported with a duration of ∼4 days, although both the beginning and end of the bright phase of the event are missed since they fall in the blind periods mentioned above. We adopt 6 days as a conservative duration for the event (above the detection threshold) – that is, one day before and one day after the observed window. This is at the low end of the estimated duration of these events, as discussed at the end of Sect. 7. Hence, the success rate of events per pointing near a critical curve is $6/30 = 0.2$. This is only a factor of a few below our expected number of 0.9 events per pointing, and is easily accommodated by small changes (consistent with the photometry) in the IMF derived from the SED model (black line in Fig. 9), or by parsec-scale variations in the distribution of SG stars in this portion of the arc. Hence, the predicted rate of 0.9 events per observation is reasonably consistent with the observed rate of 0.2 stars detected per pointing in the FrontierSN program. We discuss later how the predicted rate matches better the observed one when modifying the B/R SG ratio. Similarly, the F1 detection in the Flashlights program corresponds to a success rate of $1/2 = 0.5$ (two observations are carried out for each cluster in the Flashlights program, and F1 was seen in only one of them), which is perfectly consistent with our estimate of 0.5 lensed stars per observation in the $F200LP$ filter. Our findings are also consistent with the fact that S1 and F1 are found in regions where the macromodel predicts a magnification $\mu \approx 150$–300 for each counterimage, and the hypothesis that S1 and F1 are counterimages of one another, but are detected when each one is experiencing a microlensing event at different epochs.

As discussed above, the two events S2 and F2 can be easily interpreted in a similar way, but only if a second critical curve passes near S2 and F2 (see, for instance, the critical curve from the model of Bergamini et al. (2023) in Fig. 7, that predicts the critical curve passing closer to S2 and F2). Our current lens model does not produce such a second critical curve, but small variations in the lens model should easily produce the needed

critical curve (as already shown in Rodney et al. 2018). If no critical curve passes near S2 and F2, then these stars must be incredibly luminous in order to be detected at such low magnification factors. Their luminosities would imply the existence of stars beyond the HD limit and would create an internal inconsistency with our own predictions on S1 and F1, since if the HD limit evolves at this redshift, we would expect significantly more lensed stars than detected near S1 and F1. We consider this possibility unlikely and instead blame the lower accuracy of our lens model in this portion of the arc. Future improved lens models are needed in order to better constrain that second possible critical curve crossing. JWST data will provide further lensing constraints for the lens model.

In summary, when comparing our results with observations, our predictions exceed the number of observed lensed stars if we do not set an upper limit to the luminosity of stars with temperatures $T < 15\,000$ K. On the other hand, our predictions are in reasonable agreement with the observations if one considers that SG stars at $z = 1$ are also less luminous than the HD limit established at $z \approx 0$. Hence, our results are consistent with the hypothesis that the HD limit does not evolve between $z = 0$ and $z = 1$, and that the abundance of SG stars at $z = 1$ is consistent with local measurements.

In the results discussed up to this point, we have assumed $\delta = 0$ in Eq. (9). This can be considered as a strong assumption since it implicitly assumes that the ratio of blue SGs to red SGs (of the same luminosity) is equal to 1. For old galaxies blue SGs are expected to be very rare, while red SGs represent the evolved state of less massive (and longer lived) intermediate-mass MS stars. In this sense, we can consider δ as a parameterization of the age of the galaxy. From the SED fit to the observed photometry, and the blue color of the galaxy, we infer that the Spock galaxy is relatively young (see Sect. 6.3), or it has sufficient star formation to support the existence of blue SGs. So our choice of $\delta = 0$ is, in principle, well motivated. If blue SGs are more common than red SGs, then $\delta > 0$. For values of $\delta = 1$, the numbers for each temperature bin in Figs. 15, 16, and 18 need to be weighted not by a factor $1/5$ as done earlier, but by a factor $W = T^{\delta}/\int T^{\delta} = 0.04, 0.13, 0.19, 0.25,$ and 0.38 for the temperature bins $T = 3500$ K, $10\,000$ K, $15\,000$ K, $20\,000$ K, and $30\,000$ K, respectively. While for $\delta = -1$ the weights are 0.53, 0.19, 0.13, 0.09, and 0.06 for the same respective bins. Obviously, $W = 0.2$ for all temperatures when $\delta = 0$. The weights above assume all luminous stars are distributed in the five temperature bins. This is a simplification since in a real situation there may be stars with higher temperatures. In this work we are assuming the number of stars above $30\,000$ K is negligible. This approximation is appropriate if the B/R ratio is small (such as in the $\delta = -1$ case), but not so much if the $B/R > 1$.

For $\delta = 1$, and after imposing the HD limit, the number of predicted detections remains more or less constant in the $F814W$ filter with respect to the case $\delta = 0$, but it increases in the bluer HST's $F200LP$ filter in Table 1. For the IR JWST filter $F200W$, we observe a significant reduction. This filter is well suited for cool stars at $z = 1$, hence is very sensitive to their abundance. For $\delta = -1$ (more red SGs than blue SGs), the situation reverses, and we predict a large number of detections in $F200W$. The current statistics based on HST data do not allow us to discriminate between different values of δ, but future observations with JWST should allow us to favor one scenario over the rest.

Interestingly, the results discussed above are to first order insensitive to changes in the micromodel. As shown in Fig. 10, considering a smaller value of Σ_* has a minor impact on the probability of high-magnification events. The smaller $\Sigma_* = 5\,M_{\odot}\,\mathrm{pc}^{-2}$

results in a narrower PDF for the magnification, but its median value peaks at larger magnifications, and the tail of extreme magnification still follows the canonical μ^{-2} power law past $\mu = 1000$. These two effects compensate the smaller abundance of microlenses, especially at large magnification values.

These results are derived without taking into account specific models of stellar evolution. In particular, the relatively short lifetimes of SG stars are not being considered in this work. Instead, we have assumed that these stars must exist in the Spock galaxy to be able to interpret the observations. Our results show that the abundance of these stars is well approximated by the abundance predicted by the IMF of stars with the corresponding mass to produce such luminosities (assuming the MS M–L relation). This reasoning can be turned around to conclude that in order to have such an abundance of luminous stars, a relatively recent episode of star formation must have taken place, which is consistent with the young age derived for the Spock galaxy from SED fitting.

The results derived above assume there are no stars beyond the HD limit. Under that assumption, we find that our results are roughly consistent with the observations (that is, ~0.5 observed stars per pointing). Given the relatively small area that is being amplified in the Spock arc, we also consider the possibility that stars beyond the HD limit may exist, but their surface number density is smaller than what was assumed in our previous calculations. Otherwise these stars would have been detected by the FrontierSN or Flashlights programs, preferentially at larger distances from the critical curve. Since the observed stars appear near the expected position of the critical curves (true at least for S1 and F1, and likely true also for S2 and F2, assuming a second critical curve passes between them), we can conclude that if stars with luminosities beyond the HD limit exist in this small portion of the Spock galaxy, their number density must be smaller than what was assumed in our calculations above.

The strongest constraint on the abundance of stars beyond the HD limit comes from the regions with smallest magnification, as shown in Figs. 12 and 14. Our model assumed a surface number density of ~8000 stars kpc^{-2} with luminosities beyond $6 \times 10^5 L_\odot$. From the results in Table 1, and adopting the case $\delta = 0$, the number of expected observed stars per pointing, and beyond the HD limit is simply the difference between Column 3 (labeled "No HD$_{\delta=0}$"), and Cols. 4–6 – that is, ~3.5 for the FrontierSN program or ~4.5 for the Flashlights program. These numbers need to be reduced by approximately a factor 20 for these stars to be rare enough to not contribute significantly to the number of detections farther away from the critical curve. This translates into a surface number density of <400 stars kpc^{-2} with luminosities beyond the HD limit. If we consider the bins with magnifications 67 and 135, where these very bright stars are more likely to be found, the area in the source plane with magnification in this range is $A \approx 530 \times 20 \approx 0.01$ kpc^2. This means the number of stars beyond the HD limit in this region can be up to ~4. These stars remain in general undetected without the aid of microlensing provided they are less luminous than $L_{bol} < 3 \times 10^7 L_\odot$, as estimated earlier. Similar arguments can be used, but this time applied to the smaller area associated with the larger-magnification bins, and assuming that the stars responsible for the observed events are less luminous than the HD limit. Our model contains ~9000 stars kpc^{-2} with bolometric luminosities between ~$10^5 L_\odot$ and ~$6 \times 10^5 L_\odot$. As discussed above, this number density (equivalent to ~1 SG star per 10×10 pc^2) reproduces the observations from the FrontierSN and Flashlights programs reasonably well. Although high, this number density is consistent with the fact that SG stars are often found in large concentrations of stars (Davies et al. 2007).

The abundance of SG stars in the Spock galaxy can be better constrained with future observations of this arc. If we consider the farthest bin in Fig. 11 at $d \approx 16$ pc from the caustic (yellow bin, or total magnification $\mu \approx 70$, equivalent to regions in the image plane where $\mu \approx 35$ for each counterimage), this bin is highly sensitive to the presence of the most luminous stars (as shown more clearly in Fig. 12). By simply mapping how far from the critical curve lensed stars are observed, one can constrain the abundance of the most massive and luminous stars, since at relatively large distances from the caustic, only the most luminous stars are detectable.

Future JWST observations will improve the statistics on the number of detected lensed stars, offering us a privileged view into the massive end of the IMF of the Spock galaxy. Once enough SG stars are detected by JWST, an interesting application is to reverse engineer the tip of the red giant branch (TRGB) distance indicator and use it instead to constrain the magnification. If the TRGB holds at this redshift, we can use the observed luminosities of the brightest red stars to infer their true unlensed luminosity. This gives a direct constraint on the magnification which can be used to improve on the lens models. Current models typically disagree by a factor of 2–3 in the magnification near the critical curves. If the maximum bolometric luminosity for red SGs is still ~$6 \times 10^5 L_\odot$, JWST will be able to see these bright stars and use them as distance indicators to constrain μ. There is of course the issue of microlensing that may introduce uncertainty in the magnification, but monitoring these stars should provide accurate measurements of the mode of the magnification. These stars can also show variability, although this is expected to be different than the $1/\sqrt{t}$ variability predicted by lensing (where t is time to the maximum magnification). Frequent monitoring of these stars should easily distinguish between intrinsic variability and a microlensing event. Since JWST will be able to see red SGs farther away from the critical curve, at these separations the mode of the magnification is a good tracer of the macromodel magnification at that particular position.

Another interesting property that can be checked with future observations is to estimate the presence of luminous blue companions to red SGs. From local measurements, ~20% of the red SGs are expected to have such companions (Neugent et al. 2020a). Monitoring of microcaustic events can unambiguously reveal companion stars provided that this companion is bright enough so it can be observed when the companion crosses a microcaustic. These events would show distinctive chromatic features since the stars in the pair would have different temperatures (and colors) which manifest themselves when each star is crossing a microcaustic.

10. Conclusions

We have presented an updated model of the cluster MACS0416, based on the hybrid algorithm WSLAP+, taking advantage of new weak-lensing measurements over the extended region covered by the BUFFALO program, as well as new spectroscopically confirmed multiply lensed galaxies confirmed by MUSE data. Our new lens model contains $4.9 \times 10^{14} M_\odot$ in the central 1 Mpc. The mass adopts the same bimodal distribution found in earlier work, but we find the mass contained in each substructure to be almost identical, suggesting a mass ratio 1:1 for the structures in this cluster.

Using this lens model, we predict the number of expected multiply lensed galaxies to be detected with JWST at $z = 6$ and $z = 9$, using the latest luminosity functions at high redshift

derived from recent work based on JWST observations. For $z = 6$ we predict the usual depletion effect where, despite the increased effective depth provided by lensing, we expect fewer galaxies near the cluster center than in the parallel field, where the magnification is $\mu \approx 1$. However, at $z = 9$ the situation is reversed and we predict a larger number of $z = 9$ galaxies detected in the cluster field than in the parallel field. This is a direct consequence of the steeper luminosity function at $z = 9$ than at $z = 6$ in the faint end.

We focus our attention on four transients identified in one of the strongly lensed arcs in MACS0416, dubbed the Spock arc. Although other interpretations are still possible for these transients (Rodney et al. 2018; Kelly et al. 2022), we demonstrate that they are consistent with the hypothesis that they are due to microlensing events of SG stars at $z = 1.0054$. These microlensing events are expected to be frequent in this arc. We consider two of the HST filters (and depths) to match the real observations, the red filter $F814W$ (and observations at 28.5 AB mag depth) and the wider, but bluer, filter $F200LP$ (and a depth of 29 mag). From the lack of detection of lensed stars in most observations of this arc, we set an upper limit to the luminosity of detectable stars, ruling out the existence of SG stars with $L > 3 \times 10^6 \, L_\odot$ in the portion of the arc that is being multiply lensed. We assume the stars that are being lensed all belong to the SG type, with luminosities at least $\sim 10^5 \, L_\odot$. These stars can have a wide range of temperatures. We consider temperatures from $T = 3500$ K to $T = 30\,000$ K. The abundance of these stars is originally constrained by a model based on the Kroupa IMF that we fit to the observed photometry in different bands using BAGPIPES. We find that the predicted number of observed lensed stars matches the observations if the HD limit has no significant evolution between $z = 0$ and $z = 1$. Alternatively, stars beyond the HD limit may still exist in this portion of the galaxy, but their number density must be <400 stars kpc^{-2} in order for their probability of being observed to be sufficiently small. On the other hand, if the stars responsible for the observed events are less luminous than the HD limit but with bolometric luminosities greater than $10^5 \, L_\odot$, their surface number density must be ~ 9000 SG stars kpc^{-2}.

The four observed events can be fully described as microlensing events of SG stars. In particular, the NW S2 event is consistent with the microlensing of a blue SG star (assuming a critical curve passes nearby), while the SE event is consistent with the microlensing of a red SG star (see Fig. 1). For F1 and F2, the lack of color information does not allow us to constrain the type of star being lensed, but the filter in this case is better suited for hot stars than for red stars. The HD limit can also be connected to metallicity. We find that the metallicity of the Spock galaxy is likely supersolar. In this scenario, massive stars would lose mass more efficiently through radiation-driven stellar wind, tightening the HD limit.

An alternative way of testing for the HD limit is by measuring the separation from the microlensed events to the critical curve. Stars with luminosities beyond the HD limit can be found at larger separations since they require smaller magnification factors in order to be detected. The Spock arc is not ideal for this purpose because there is still significant uncertainty on the position of the critical curve (or even the number of them) that is (are) crossing the arc. However, under the assumption that at least one of them (between S1 and F1) is well reproduced by our lens model, we also find good consistency between the observed distance to the critical curve of the microlensed events and the existence of an HD limit.

We also make predictions for future JWST observations of this cluster. We find that in the $F200W$ filter ($\sim 2\,\mu$m), JWST detects ~ 5 SG stars per observation spread along the Spock arc.

We have shown how there is a high variability in the number of expected detected stars depending on the depth of the observation (or redshift of the background source), the filter used to perform the observation, the temperature of the lensed stars, and obviously the luminosity of the stars and their age. Each particular arc and observation needs to be modeled specifically. Other arcs in the same cluster (as well as in other clusters) have similar events (see Kelly et al. 2022; Meena et al. 2023a, for events discovered as part of the Flashlights program). The JWST predictions made in this work are consistent with recent findings based on actual JWST observations of this arc by Yan et al. (2023), and they were made public after submission of this work. In particular, our predictions imply the validity of the HD limit at $z = 1$ based on the observed JWST detection rate of approximately one event per pointing in this arc reported by Yan et al. (2023). Future observations of this cluster with JWST are expected to detect even more events that will allow better constraints on the abundance of SG stars in the Spock galaxy at $z \approx 1$.

References

Bacon, R., Accardo, M., Adjali, L., et al. 2010, SPIE Conf. Ser., 7735, 773508
Bergamini, P., Grillo, C., Rosati, P., et al. 2023, A&A, 674, A79
Bertin, E., & Arnouts, S. 1996, A&AS, 117, 393
Bessell, M., & Murphy, S. 2012, PASP, 124, 140
Bowler, R. A. A., Dunlop, J. S., McLure, R. J., et al. 2015, MNRAS, 452, 1817
Caminha, G. B., Grillo, C., Rosati, P., et al. 2017, A&A, 600, A90
Carnall, A. C., McLure, R. J., Dunlop, J. S., & Davé, R. 2018, MNRAS, 480, 4379
Chen, Y., Bressan, A., Girardi, L., et al. 2015, MNRAS, 452, 1068
Chen, W., Kelly, P. L., Diego, J. M., et al. 2019, ApJ, 881, 8
Chen, W., Kelly, P. L., Treu, T., et al. 2022, ApJ, 940, L54
Coelho, P. R. T. 2014, MNRAS, 440, 1027
Davies, B., Figer, D. F., Kudritzki, R.-P., et al. 2007, ApJ, 671, 781
Davies, B., Crowther, P. A., & Beasor, E. R. 2018, MNRAS, 478, 3138
Diego, J. M. 2019, A&A, 625, A84
Diego, J. M. 2022, A&A, 665, A127
Diego, J. M., Protopapas, P., Sandvik, H. B., & Tegmark, M. 2005, MNRAS, 360, 477
Diego, J. M., Tegmark, M., Protopapas, P., & Sandvik, H. B. 2007, MNRAS, 375, 958
Diego, J. M., Broadhurst, T., Molnar, S. M., Lam, D., & Lim, J. 2015, MNRAS, 447, 3130
Diego, J. M., Broadhurst, T., Chen, C., et al. 2016, MNRAS, 456, 356
Diego, J. M., Kaiser, N., Broadhurst, T., et al. 2018, ApJ, 857, 25
Diego, J. M., Pascale, M., Kavanagh, B. J., et al. 2022, A&A, 665, A134

Diego, J. M., Meena, A. K., Adams, N. J., et al. 2023, A&A, 672, A3
Dohm-Palmer, R. C., & Skillman, E. D. 2002, AJ, 123, 1433
Duric, N. 2004, Advanced Astrophysics (Cambridge University Press), 1
Eggenberger, P., Meynet, G., & Maeder, A. 2002, A&A, 386, 576
Ekström, S., Georgy, C., Eggenberger, P., et al. 2012, A&A, 537, A146
Gilkis, A., Shenar, T., Ramachandran, V., et al. 2021, MNRAS, 503, 1884
Harikane, Y., Ouchi, M., Oguri, M., et al. 2023, ApJS, 265, 5
Harvey, D., Robertson, A., Tam, S.-I., et al. 2021, MNRAS, 500, 2627
Hinton, S. R., Davis, T. M., Lidman, C., Glazebrook, K., & Lewis, G. F. 2016, Astron. Comput., 15, 61
Hoag, A., Huang, K. H., Treu, T., et al. 2016, ApJ, 831, 182
Horne, K. 1986, PASP, 98, 609
Humphreys, R. M. 1978, ApJS, 38, 309
Humphreys, R. M. 1983, ApJ, 269, 335
Ishigaki, M., Kawamata, R., Ouchi, M., et al. 2018, ApJ, 854, 73
Jauzac, M., Clément, B., Limousin, M., et al. 2014, MNRAS, 443, 1549
Jauzac, M., Jullo, E., Eckert, D., et al. 2015, MNRAS, 446, 4132
Johnson, T. L., Sharon, K., Bayliss, M. B., et al. 2014, ApJ, 797, 48
Kaurov, A. A., Dai, L., Venumadhav, T., Miralda-Escudé, J., & Frye, B. 2019, ApJ, 880, 58
Kawamata, R., Oguri, M., Ishigaki, M., Shimasaku, K., & Ouchi, M. 2016, ApJ, 819, 114
Kayser, R., Refsdal, S., & Stabell, R. 1986, A&A, 166, 36
Kelly, P. L., Diego, J. M., Rodney, S., et al. 2018, Nat. Astron., 2, 334
Kelly, P., Acebron, A., Alfred, A., et al. 2019, Flashlights: Many Extremely Magnified Individual Stars as Probes of Dark Matter and Stellar Populations to Redshift z 2, HST Proposal, Cycle 27, ID #15936
Kelly, P. L., Chen, W., Alfred, A., et al. 2022, arXiv e-prints [arXiv:2211.02670]
Kochanek, C. S. 2004, ApJ, 605, 58
Koekemoer, A. M., Faber, S. M., Ferguson, H. C., et al. 2011, ApJS, 197, 36
Lagattuta, D. J., Richard, J., Bauer, F. E., et al. 2022, MNRAS, 514, 497
Langer, N., & Maeder, A. 1995, A&A, 295, 685
Lotz, J. M., Koekemoer, A., Coe, D., et al. 2017, ApJ, 837, 97
Mahler, G., Sharon, K., Fox, C., et al. 2019, ApJ, 873, 96
Mahler, G., Jauzac, M., Richard, J., et al. 2023, ApJ, 945, 49
Mann, A. W., & Ebeling, H. 2012, MNRAS, 420, 2120
Massey, P., Neugent, K. F., Ekström, S., Georgy, C., & Meynet, G. 2023, ApJ, 942, 69
McDonald, S. L. E., Davies, B., & Beasor, E. R. 2022, MNRAS, 510, 3132
McLeod, D. J., McLure, R. J., Dunlop, J. S., et al. 2015, MNRAS, 450, 3032
Meena, A. K., Arad, O., & Zitrin, A. 2022, MNRAS, 514, 2545
Meena, A. K., Zitrin, A., Jiménez-Teja, Y., et al. 2023a, ApJ, 944, L6
Meena, A. K., Chen, W., Zitrin, A., et al. 2023b, MNRAS, 521, 5224
Miralda-Escude, J. 1991, ApJ, 379, 94
Montes, M. 2022, Nat. Astron., 6, 308
Mosquera, A. M., & Kochanek, C. S. 2011, ApJ, 738, 96
Nagai, D., Kravtsov, A. V., & Vikhlinin, A. 2007, ApJ, 668, 1
Neira, F., Anguita, T., & Vernardos, G. 2020, MNRAS, 495, 544
Neugent, K. F., Massey, P., Georgy, C., et al. 2020a, ApJ, 889, 44
Neugent, K. F., Levesque, E. M., Massey, P., Morrell, N. I., & Drout, M. R. 2020b, ApJ, 900, 118
Niemiec, A., Jauzac, M., Eckert, D., et al. 2023, MNRAS, 524, 2883
Oesch, P. A., Bouwens, R. J., Illingworth, G. D., et al. 2015, ApJ, 808, 104
Oguri, M., Diego, J. M., Kaiser, N., Kelly, P. L., & Broadhurst, T. 2018, Phys. Rev. D, 97, 023518
Oke, J. B., & Gunn, J. E. 1983, ApJ, 266, 713
Palencia, J. M., Diego, J. M., Kavanagh, B. J., & Martinez, J. 2023, arXiv e-prints [arXiv:2307.09505]
Pascale, M., Frye, B. L., Diego, J., et al. 2022, ApJ, 938, L6
Pérez-González, P. G., Costantin, L., Langeroodi, D., et al. 2023, ApJ, 951, L1
Piqueras, L., Conseil, S., Shepherd, M., et al. 2019, ASP Conf. Ser., 521, 545
Richard, J., Claeyssens, A., Lagattuta, D., et al. 2021, A&A, 646, A83
Rodney, S. 2014, Frontier Field Supernova Search, HST Proposal, Cycle 22, ID #13790
Rodney, S. A., Balestra, I., Bradac, M., et al. 2018, Nat. Astron., 2, 324
Schaller, G., Schaerer, D., Meynet, G., & Maeder, A. 1992, A&AS, 96, 269
Schechter, P. L., & Wambsganss, J. 2002, ApJ, 580, 685
Schechter, P. L., Wambsganss, J., & Lewis, G. F. 2004, ApJ, 613, 77
Seitz, C., & Schneider, P. 1997, A&A, 318, 687
Sendra, I., Diego, J. M., Broadhurst, T., & Lazkoz, R. 2014, MNRAS, 437, 2642
Steidel, C. C., Adelberger, K. L., Giavalisco, M., Dickinson, M., & Pettini, M. 1999, ApJ, 519, 1
Steinhardt, C. L., Jauzac, M., Acebron, A., et al. 2020, ApJS, 247, 64
Umetsu, K. 2020, A&ARv, 28, 7
Umetsu, K., Sereno, M., Medezinski, E., et al. 2015, ApJ, 806, 207
Venumadhav, T., Dai, L., & Miralda-Escudé, J. 2017, ApJ, 850, 49
Vernardos, G., Fluke, C. J., Bate, N. F., & Croton, D. 2014, ApJS, 211, 16
Wagle, G. A., Ray, A., & Raghu, A. 2020, ApJ, 894, 118
Weilbacher, P. M., Palsa, R., Streicher, O., et al. 2020, A&A, 641, A28
Welch, B., Coe, D., Diego, J. M., et al. 2022, Nature, 603, 815
Williams, H., Kelly, P. L., Chen, W., et al. 2023, Science, 380, 416
Yan, H., Ma, Z., Sun, B., et al. 2023, ApJS, 269, 43
Zitrin, A., Meneghetti, M., Umetsu, K., et al. 2013, ApJ, 762, L30

Appendix A: WSLAP+

To optimize the lens model we use the code WSLAP+ (Diego et al. 2005, 2007; Sendra et al. 2014; Diego et al. 2016). A lens model derived using WSLAP+ is considered a hybrid type of model as it combines a free-form decomposition of the lens plane for the smooth large-scale component with a small-scale contribution from the member galaxies. The code combines weak and strong lensing in a natural way, with changes made in the large-scale and small-scale components impacting equally the strong- and weak-lensing observables. Details can be found in the references above. Here we give a brief description of the method.

We start with the classic definition of the lens equation

$$\beta = \theta - \alpha(\theta, \Sigma), \tag{A.1}$$

where θ is the observed position of the source, α is the deflection angle, $\Sigma(\theta)$ is the unknown surface mass density of the cluster at the position θ, and β is the unknown position of the background source. The optimization of the WSLAP+ solution takes advantage of the fact that the lens equation can be expressed as a linear function of the surface mass density, Σ. WSLAP+ parameterizes Σ as a linear superposition of functions, which translates into $\alpha(\theta, \Sigma)$ also being linear in Σ.

In WSLAP+, Σ is described by the combination of two components: (i) a smooth component (usually parameterized as superposition of Gaussians) corresponding to the free-form part of the model, or large-scale cluster potential, and (ii) a compact component that accounts for the mass associated with individual galaxies in the cluster. For the smooth component, we use Gaussian functions defined over a grid of points. A Gaussian function is simple, and enables fast computation of the deflection field, but also provides a good compromise between the desired compactness and smoothness of the basis function. The grid configuration can be defined as regular (all grid points have the same size) or irregular (grid points near the center are in general smaller). Adopting a regular grid is similar to a flat prior in the mass distribution, while an irregular grid can be interpreted as a model with a prior on the mass distribution with higher mass density assigned to smaller cells. For this work, we use a dynamical (irregular) grid with increased resolution in the central region, where strong-lensing constraints are present. In particular, we consider a grid with 745 points. The distribution of grid points is obtained from a Monte Carlo realization of the mass density previously obtained with a regular grid. The final distribution of points is more concentrated around the two brightest cluster galaxies (BCGs), with the density of grid points being smallest in the outskirts of the 6×6 arcmin^2 region.

For the compact component, we directly adopt the light distribution in HST's F160W band around the brightest member elliptical galaxies in the cluster, and spectroscopically confirmed (by MUSE) members. For each galaxy, we assign a mass proportional to its surface brightness. This mass is the only free parameter, and it is later readjusted as part of the optimization process. The number of parameters connected with the compact component depends on the number of adopted layers. Each layer contains a number of member galaxies. The minimum number of layers is 1, corresponding to the case where all galaxies are placed in the same layer — that is, they are all assumed to have the same mass-to-light ratio. In this case, the single layer is proportional to the light distribution of all member galaxies, and is assigned a fiducial mass accounting for the total mass of member galaxies. For each layer there is one extra parameter which accounts for the renormalization constant multiplying the map of the mass distribution. This renormalization parameter is later optimized by WSLAP+. For the particular case of MACS0416, we use four layers. The first two layers contain the two main BCGs, the third layer contains red-sequence member galaxies, and the fourth layer contains spectroscopically confirmed member galaxies which are not in the red sequence and hence may have a different mass-to-light ratio.

As shown by Diego et al. (2005, 2007), the strong- and weak-lensing problem can be expressed as a system of linear equations that can be represented in a compact form,

$$\mathbf{\Theta} = \mathbf{\Gamma} X, \tag{A.2}$$

where the measured strong- and weak-lensing observables are arranged in $\mathbf{\Theta}$ of dimension $N_\Theta = 2N_{sl} + 2N_{wl}$ (where N_{sl} and N_{wl} are the strong- and weak-lensing observables, each contributing with two constraints). The unknown surface mass density and source positions are in the array X of dimension

$$N_X = N_c + N_l + 2N_s. \tag{A.3}$$

The array X also contains the $N_l = 4$ unknown renormalization factors associated with the four layers. N_c is the number of grid points (or cells) that we use to divide the field of view, and N_s is the number of background sources being strongly lensed (each source contributes with two variables, β_x and β_y). Finally, the matrix $\mathbf{\Gamma}$ is known (for a given grid configuration and fiducial galaxy deflection field) and has dimension $N_\Theta \times N_X$.

The solution, X, of the system of Eq. (A.2) is found after minimizing a quadratic function of X (derived from the system of Eq. (A.2) as described by Diego et al. 2005). A detailed discussion of the algorithm used to solve the system of linear equations is given by Diego et al. (2005). For a discussion of its convergence and performance (based on simulated data), we refer the reader to Sendra et al. (2014).

Appendix B: Arc positions and redshifts

Strong lensing constraints used to derive the lens model. ID$_2$ and z_2 are the IDs and redshifts in Bergamini et al. (2023). In general, all redshifts agree to the subpercent level, except for our system (ID = 42) where Bergamini et al. (2023) derives a redshift 14.5% larger. Arcs marked with † are from Bergamini et al. (2023), and are not included in our set of constraints since they were published after the model was derived. Arcs that have no ID$_2$ nor z_2 in the table are systems identified with BUFFALO and MUSE data that are included in our model, but are not included by Bergamini et al. (2023). These are systems ID = 33, 38, 40, 43, 44, 46, 50, 53, 54, 55, 70, and 72.

Table B.1. Full strong lensing dataset.

ID	RA	DEC	z_{MUSE}	ID$_2$	z_2
1	64.0408675	-24.0616447	1.896	5.1c	1.893
1	64.0435396	-24.0635339	-	5.1b	1.893
1	64.0474367	-24.0686997	-	5.1a	1.893
2	64.0411592	-24.0618356	1.895	5.2c	1.893
2	64.0431533	-24.0631203	-	5.2b	1.893
2	64.0475325	-24.0688519	-	5.4a	1.893
3	64.0308421	-24.0671572	1.9894	15.1c	1.990
3	64.0353283	-24.0710203	-	15.1b	1.990
3	64.0418754	-24.0757592	-	15.1a	1.990
4	64.0308492	-24.0672517	1.99	15.2c	1.990
4	64.0352429	-24.0710325	-	15.2b	1.990
4	64.0419121	-24.0758594	-	15.2a	1.990
5	64.0324804	-24.0684442	2.0948	16.1c	2.095
5	64.0327321	-24.0686961	-	16.1b	2.095
5	64.0335933	-24.0694772	-	16.1a	2.095
5	64.0436363	-24.0769933	-	-	
6	64.0398687	-24.0631192	2.0881	7c	2.085
6	64.0407412	-24.0636225	-	7b	2.085
6	64.0471708	-24.0711372	-	7a	2.085
7	64.0261300	-24.0772783	2.2982	29c	2.298
7	64.0284838	-24.0797714	-	29b	2.298
7	64.0367787	-24.0839397	-	29a	2.298
8	64.0393337	-24.0704250	1.0054	13a	1.005
8	64.0383658	-24.0697531	-	13b	1.005
8	64.0343062	-24.0660503	-	13c	1.005
9	64.0276462	-24.0727036	3.2175	20.1c	3.222
9	64.0322367	-24.0751339	-	20.1b	3.222
9	64.0404263	-24.0815053	-	20.1a	3.222
10	64.0263242	-24.0743661	1.6333	24c	1.637
10	64.0311150	-24.0789806	-	24b	1.637
10	64.0359133	-24.0813494	-	24a	1.637
11	64.0241529	-24.0809203	1.9656	36c	1.964
11	64.0284129	-24.0845719	-	36b	1.964
11	64.0316896	-24.0857892	-	36a	1.964
12	64.0235546	-24.0817486	2.2182	37c	2.218
12	64.0286679	-24.0860025	-	37b	2.218
12	64.0298979	-24.0863944	-	37a	2.218
13	64.0344096	-24.0637628	2.0910	10c	2.093
13	64.0396529	-24.0666592	-	10b	2.0943
13	64.0446321	-24.0721236	-	10a	2.093
14	64.0465296	-24.0604303	3.2355	1c	3.238
14	64.0470354	-24.0608272	-	1b	3.238
14	64.0491533	-24.0628947	-	1a	3.238
15	64.0422746	-24.0605783	2.1067	4c	2.107
15	64.0475379	-24.0660783	-	4b	2.107
15	64.0481908	-24.0669914	-	4a	2.107
16	64.0365775	-24.0670578	0.9397	12.1c	0.940
16	64.0369150	-24.0674903	-	12.1b	0.940
16	64.0409596	-24.0712164	-	-	
17	64.0230608	-24.0772986	5.3659	32c	5.365
17	64.0284821	-24.0830294	-	32b	5.365
17	64.0351254	-24.0855331	-	32a	5.365
18	64.0293633	-24.0733550	5.1060	21.1c	5.106
18	64.0308662	-24.0742067	-	21.1b	5.106
19	64.0250233	-24.0750497	3.4909	27c	3.492
19	64.0294879	-24.0799181	-	27b	3.492
19	64.0375504	-24.0836828	-	27a	3.492

Table B.1. cont.

ID	RA	DEC	z_{MUSE}	ID$_2$	z_2
20	64.0227721	-24.0746250	3.4406	30c	3.440
20	64.0313208	-24.0819283	-	30b	3.440
20	64.0337146	-24.0832186	-	30a	3.440
21	64.0416350	-24.0600322	3.2885	3c	3.290
21	64.0453321	-24.0627914	-	3b	2.290
21	64.0493079	-24.0682117	-	3a	3.290
22†	64.0383500	-24.0841261	3.253	28a	3.253
22	64.0264042	-24.0767289	3.2526	28c	3.253
22	64.0284067	-24.0790322	-	28b	3.253
23	64.0234888	-24.0761606	4.1218	31c	4.122
23	64.0293129	-24.0818383	-	31b	4.122
23	64.0355646	-24.0847072	-	31a	4.122
24	64.0269333	-24.0699764	3.8696	-	
24	64.0340133	-24.0745969	3.8710	18b	3.871
24	64.0402579	-24.0798950	-	18a	3.871
25	64.0266083	-24.0705319	4.1032	19.1c	4.103
25	64.0337633	-24.0748514	-	19.1b	4.103
25	64.0401517	-24.0803403	-	19.1a	4.103
26†	64.0468408	-24.0753850	3.292	11a	3.292
26	64.0353038	-24.0647647	3.2922	11c	3.292
26	64.0385875	-24.0659972	-	11b	3.292
27	64.0252696	-24.0736092	3.0773	26c	3.081
27	64.0305596	-24.0792475	-	26b	3.081
27	64.0377979	-24.0824158	-	26a	3.081
28	64.0255200	-24.0736789	3.1103	25c	3.111
28	64.0304467	-24.0790472	-	25b	3.111
28	64.0381496	-24.0824269	-	25a	3.111
29	64.0345663	-24.0669883	3.2215	14.1a	3.221
29	64.0342617	-24.0665167	-	14.1b	3.221
29	64.0340392	-24.0669400	3.2240	14.1d	3.221
29	64.0461275	-24.0768133	-	14.1f	3.221
29	64.0340812	-24.0664786	3.2215	14.1c	3.221
30	64.0401537	-24.0667703	3.2882	9.1b	3.292
30	64.0451842	-24.0723725	-	9.1a	3.292
31	64.0436462	-24.0590344	6.1452	2.1c	6.145
31	64.0509446	-24.0665642	-	2.1a	6.145
31	64.0479096	-24.0620906	6.1480	2.1b	6.145
32	64.0377496	-24.0607753	3.6065	6c	3.607
32	64.0437075	-24.0644186	-	6b	3.607
32	64.0478788	-24.0701956	-	6a	3.607
33	64.0272008	-24.0736031	3.9230	-	
33	64.0310679	-24.0772083	-	-	
33	64.0312446	-24.0770633	-	-	
34	64.0247004	-24.0714867	2.5420	-	
34	64.0327150	-24.0785378	2.5425	23b	2.542
34	64.0357392	-24.0799517	-	23a	2.542
35	64.0309054	-24.0837350	5.9729	33b	5.973
35	64.0321100	-24.0842606	-	33a	5.973
36	64.0238171	-24.0785033	3.9228	34c	3.923
36	64.0277029	-24.0826383	-	34b	3.923
37	64.0222117	-24.0773086	5.6380	35c	5.638
37	64.0287462	-24.0842464	-	35b	5.638
37	64.0338062	-24.0857294	-	35a	5.638
38	64.0269388	-24.0757711	2.3355	-	
38	64.0295250	-24.0786211	2.3340	-	
38	64.0383083	-24.0830053	-	-	
39	64.0272463	-24.0682528	3.9680	17c	3.966

Table B.1. cont.

ID	RA	DEC	z_{MUSE}	ID_2	z_2
39	64.0351867	-24.0738864	-	17b	3.996
39	64.0405671	-24.0784167	-	17a	3.966
40	64.0251204	-24.0833403	2.2210	-	
40	64.0261767	-24.0842808	-	-	
40	64.0309450	-24.0867550	-	-	
41	64.0409938	-24.0629858	2.2430	203c	2.245
41	64.0411571	-24.0630958	-	203b	2.245
42	64.0366754	-24.0661542	1.8270	202.2c	2.091
42	64.0369308	-24.0663756	-	202.2b	2.091
43	64.0291179	-24.0667792	1.9530	-	
43	64.0375096	-24.0731747	-	-	
43	64.0386171	-24.0739053	-	-	
44	64.0238937	-24.0776206	1.8178	-	
44	64.0305688	-24.0827056	-	-	
44	64.0325083	-24.0837817	-	-	
45	64.0377446	-24.0610592	4.1138	103c	4.115
45	64.0429642	-24.0639314	-	103b	4.115
45	64.0482517	-24.0709208	-	103a	4.115
46	64.0258396	-24.0722631	2.2800	-	
46	64.0329717	-24.0770292	-	-	
46	64.0377117	-24.0805028	-	-	
47	64.0362746	-24.0606817	2.9220	107c	2.921
47	64.0448367	-24.0667225	-	107b	2.921
47	64.0461029	-24.0688289	-	107a	2.921
48	64.0400717	-24.0666814	3.2883	9.2b	3.292
48	64.0454287	-24.0725575	-	9.2a	3.292
49	64.0343333	-24.0630317	2.2810	8c	2.282
49	64.0405508	-24.0663597	-	8b	2.282
49	64.0447008	-24.0715192	-	8a	2.282
50	64.0268658	-24.0692417	3.2195	-	
50	64.0348675	-24.0746150	-	-	
50	64.0397671	-24.0788958	-	-	
51	64.0378375	-24.0598592	4.1150	106c	4.116
51	64.0459412	-24.0658472	-	106b	4.116
51	64.0477708	-24.0686717	-	106a	4.116
52	64.0239225	-24.0750281	3.2910	204c	3.291
52	64.0301767	-24.0809514	-	204b	3.291
52	64.0357446	-24.0836114	-	204a	3.291
53	64.0262950	-24.0760453	2.9259	-	
53	64.0289225	-24.0791542	-	-	
54	64.0267154	-24.0747042	2.2300	-	
54	64.0302275	-24.0786061	-	-	
54	64.0381763	-24.0823422	-	-	
55	64.0263417	-24.0687342	5.1060	-	
55	64.0349887	-24.0746083	-	-	
55	64.0401338	-24.0791333	-	-	
56	64.0366617	-24.0633144	4.3000	101c	4.299
56	64.0397071	-24.0642781	-	101b	4.299
56	64.0480804	-24.0742222	-	101a	4.299
57	64.0256154	-24.0713078	4.5018	207c	4.502

Table B.1. cont.

ID	RA	DEC	z_{MUSE}	ID_2	z_2
57	64.0331017	-24.0760244	-	207b	4.502
57	64.0393000	-24.0813358	-	207a	4.502
58†	64.0235629	-24.0731711	3.715	205c	3.715
58	64.0311558	-24.0803381	3.7153	205b	3.715
58	64.0360404	-24.0825781	-	205a	3.715
59	64.0311383	-24.0643317	4.0690	-	
59	64.0373113	-24.0697069	-	104b	4.070
59	64.0439900	-24.0750847	-	104a	4.070
60†	64.0493708	-24.0710067	6.145	112a	6.145
60	64.0389625	-24.0606803	6.1470	112c	6.145
60	64.0433679	-24.0629836	-	112b	6.145
61†	64.0508671	-24.0664261	6.145	2.2a	6.145
61	64.0434875	-24.0589444	6.1480	2.2c	6.145
61	64.0482517	-24.0624331	6.1452	2.2b	6.145
62	64.0335671	-24.0650447	4.6090	108c	4.607
62	64.0369179	-24.0680367	-	-	
62†	64.0366592	-24.0680269	4.607	108b alt	4.607
62	64.0465858	-24.0762047	4.6090	108a	4.607
63	64.0333479	-24.0674986	1.1472	201c	1.147
63	64.0404400	-24.0730881	-	201a	1.147
64	64.0338125	-24.0657972	4.0707	105c	4.071
64	64.0360046	-24.0678972	-	105b	4.071
64	64.0464792	-24.0767511	-	105a	4.071
65	64.0392596	-24.0698083	4.3000	110b	4.298
65	64.0427467	-24.0721897	-	110a	4.298
66	64.0407246	-24.0591806	5.0996	209c	5.100
66	64.0468725	-24.0638661	-	209b	5.100
66	64.0496512	-24.0680561	-	209a	5.0996
67	64.0399400	-24.0669239	5.9980	113b	5.995
67	64.0459558	-24.0740589	-	113a	5.995
68	64.0364992	-24.0622758	6.0664	102c	6.064
68	64.0411162	-24.0641319	-	102b	6.064
68	64.0484808	-24.0735939	-	102a	6.064
69	64.0378317	-24.0688725	2.9911	109b	2.989
69	64.0438154	-24.0737064	-	109a	2.989
70	64.0289792	-24.0755694	3.0750	-	
70	64.0296996	-24.0762108	-	-	
71	64.0247200	-24.0771819	4.5300	208c	4.530
71	64.0277733	-24.0806775	-	208b	4.530
72	64.0308846	-24.0837572	5.9730	-	
72	64.0320288	-24.0842872	-	-	
73†	64.0455825	-24.0727003	3.2920	9.3a	3.29
73†	64.0400004	-24.0666450	3.2920	9.3b	3.29
74†	64.0507508	-24.0658519	6.1490	210a	6.149
74†	64.0472208	-24.0611967	6.1490	210b	6.149
74†	64.0445658	-24.0593369	6.1490	210c	6.149
75†	64.0414950	-24.0626300	6.1490	210.4b	6.149
75†	64.0401050	-24.0618739	6.1490	210.4c	6.149
76†	64.0458967	-24.0602003	6.6290	211b	6.629
76†	64.0456046	-24.0600436	6.6290	211c	6.629